AGU PUBLICATIONS

JGR

Journal of Geophysical Research: Solid Earth

RESEARCH ARTICLE
10.1002/2016JB013284

Key Points:
- Isotopically enriched normal mid-ocean ridge basalts were found at 50°28′E, Southwest Indian Ridge, with the 10 km thick crust
- They formed by remelting of the Crozet hotspot materials with previous melt extraction during upslope flow to the ridge
- Isotopically enriched normal mid-ocean ridge basalts are possible chemical consequences of off-axis plume-ridge interaction globally

Supporting Information:
- Supporting Information S1
- Data Sets S1–S3

Correspondence to:
T.-P. Zhao,
tpzhao@gig.ac.cn

Citation:
Yang, A. Y., T.-P. Zhao, M.-F. Zhou, and X.-G. Deng (2017), Isotopically enriched N-MORB: A new geochemical signature of off-axis plume-ridge interaction—A case study at 50°28′E, Southwest Indian Ridge, *J. Geophys. Res. Solid Earth*, *122*, 191–213, doi:10.1002/2016JB013284.

Received 17 JUN 2016
Accepted 4 DEC 2016
Accepted article online 9 DEC 2016
Published online 18 JAN 2017

Isotopically enriched N-MORB: A new geochemical signature of off-axis plume-ridge interaction—A case study at 50°28′E, Southwest Indian Ridge

A. Y. Yang[1], T.-P. Zhao[1], M.-F. Zhou[2], and X.-G. Deng[3]

[1]Key Laboratory of Mineralogy and Metallogeny, Guangzhou Institute of Geochemistry, Chinese Academy of Sciences, Guangzhou, China, [2]Department of Earth Sciences, University of Hong Kong, Hong Kong, [3]Guangzhou Marine Geological Survey, Guangzhou, China

Abstract Interaction between the Southwest Indian Ridge (46°E and 52°20′E) and Crozet hotspot has been proposed by geophysical studies but remains controversial mostly due to the lack of E-MORB (enriched mid-ocean ridge basalts). Forty-seven new samples collected from this region, including 15 from segment 27 centered at 50°28′E with a 10 km thick crust, are all N-MORB (normal MORB) and can be classified into two groups: a high-Al group only at 50°28′E and a Main group widespread. The former, with higher Al_2O_3 and lower TiO_2 and SiO_2, have slightly enriched Sr-Nd-Hf-Pb isotopic compositions. We propose that their major and trace elemental signatures were modified by reaction with primitive cumulate in the crust, whereas the enriched isotopic compositions indicate the contribution of Crozet plume materials. During upslope flow of the Crozet plume to the ridge, decompression melting would occur along the path, which would deplete the plume in incompatible elements but not significantly change the isotopic compositions. Thus, when they finally reach the ridge, the depleted residue would remelt due to further decompression at MOR and produce isotopically enriched N-MORB at segment 27. Isotopically enriched N-MORB are known elsewhere, mostly at slower-spreading ridges possibly influenced by plumes with large plume-ridge distances. In particular, the constant Nd isotopic compositions with decreasing $(La/Sm)_N$ ratios for off-axis magmatism between the Réunion hotspot toward the CIR perfectly match such a plume-ridge interaction model. Therefore, aside from E-MORB, isotopically enriched N-MORB can also be considered as the geochemical signature for off-axis plume-ridge interaction.

1. Introduction

Hotspots and mid-ocean ridges (MOR) are two major surface manifestations of mantle upwelling and magma generation on Earth. Interaction of the two systems produces geophysical and geochemical anomalies along 15–20% of the global MOR network [*Ito et al*., 2003]. The presence of E-MORB (mid-ocean ridge basalts with enrichments in light rare earth elements (LREEs)) at MOR, in particular, has long been considered to be the necessary geochemical evidence for plume-ridge interactions [e.g., *Cushman et al*., 2004; *Ito et al*., 2003; *le Roux et al*., 2002; *Schilling*, 1973; *Schilling et al*., 1983], because plume materials are normally more enriched in both trace elements and isotopic compositions than the source of N-MORB (normal MORB). However, by compiling global MORB data at segment scales, *Gale et al*. [2013a] found that MORB erupted on the ridge segments within 200 km of hotspots do not always show obvious E-MORB signatures, which complicate our understanding on the geochemical expressions of plume-ridge interactions. Therefore, is E-MORB the only possible geochemical consequence of such interaction? Alternatively, isotopically enriched N-MORB in this study, combined with MORB of such kind worldwide, would potentially provide a new perspective on our understanding of plume-ridge interactions.

The ultraslow-spreading Southwest Indian Ridge (SWIR), in particular, is known to interact with the Bouvet and Marion hotspots which are relatively close to the SWIR (~33 km and 250 km, respectively) [*Georgen et al*., 2001; *Janney et al*., 2005; *Mahoney et al*., 1992]. However, whether the Crozet hotspot, located about 900 km south of the SWIR (Figure 1a), interacted with the ridge has been controversial, largely due to the lack of E-MORB as the direct geochemical evidence.

There is a bathymetric high and a mantle Bouguer anomaly (MBA) low between the Indomed (IFZ) and Gallieni (GFZ) fracture zones (46°E and 52°20′E, Figure 1a) [*Georgen et al*., 2001]. At 50°28′E with the shallowest water depth and the only axial high along this region (Figure 1b), seismic studies indicate the thickest oceanic

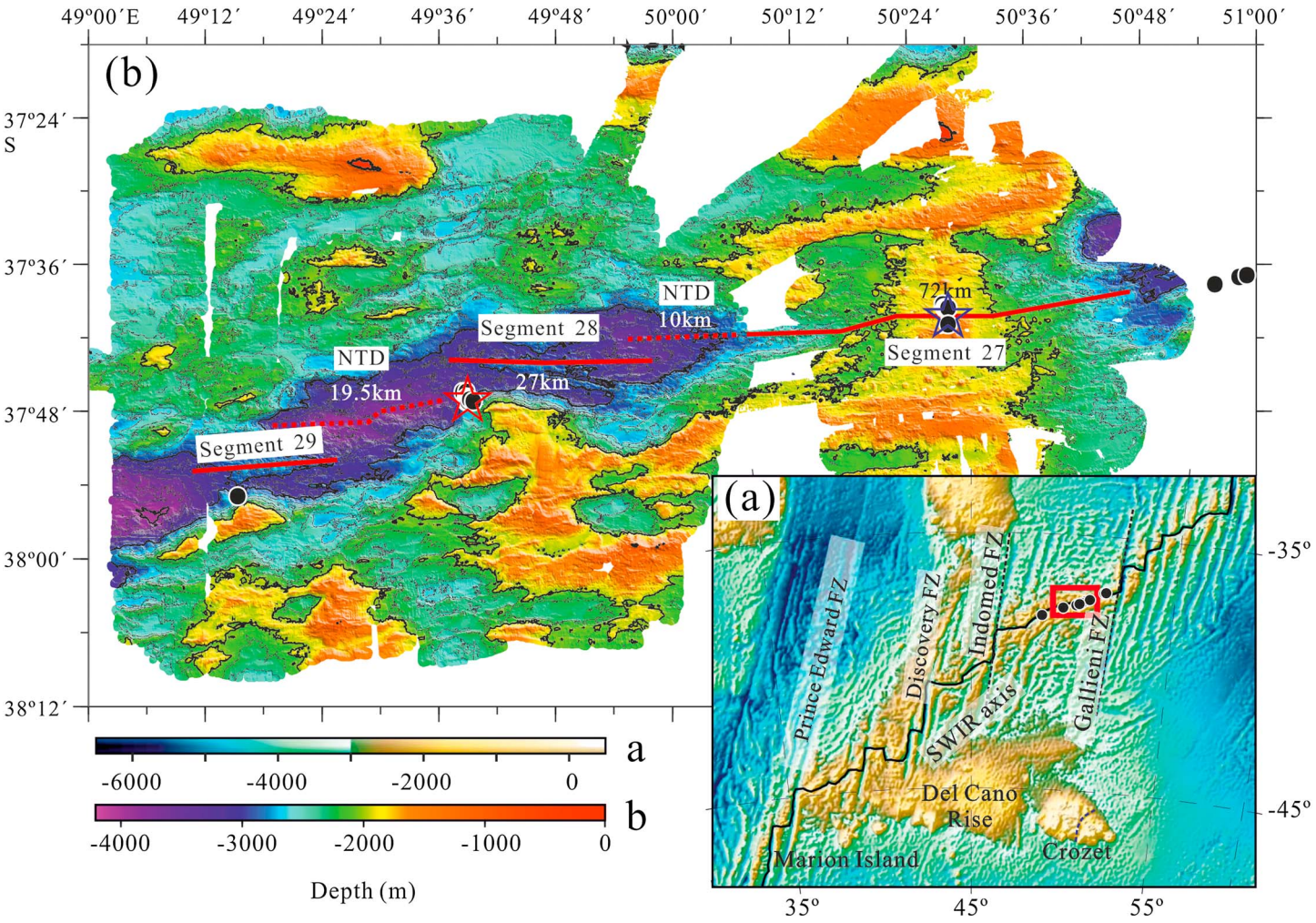

Figure 1. (a) Bathymetry map of the central Southwest Indian Ridge (SWIR), fracture zones (FZ), and off-axis high-topography edifices modified from *Li et al.* [2015]. Black dots represent sample locations in this study. Crozet Archipelago is located ~900 km south of the Indomed and Gallieni FZs (IFZ-GFZ, denoted by the black dashed lines). Blue dashed line represents the basin separating the Crozet Archipelago into western and eastern islands [*Breton et al.*, 2013]. Red rectangle marks the area shown in Figure 1b. (b) High-resolution bathymetry map of 49–51°E derived from the multibeam data from *Niu et al.* [2015] with detailed locations of most samples (four samples plot out of the map area). The red solid and dashed lines indicate the spreading segments and the nontransform discontinuities (NTDs), respectively [*Cannat et al.*, 1999; *Sauter et al.*, 2001]. The red star represents the Dragon Flag active vent field at segment 28, and the blue star represents an inactive hydrothermal vent at segment 27 [*Tao et al.*, 2012].

crust along ultraslow-spreading ridges [*Carbotte et al.*, 2015] up to 10 km thick [*Niu et al.*, 2015] and off axis [*Li et al.*, 2015], suggesting that robust magmatism at this particular location has lasted at least 3 Ma [*Li et al.*, 2015]. Off-axis topographic and gravimetric studies further extend such a melting anomaly to persist for 10 Ma [*Sauter et al.*, 2009]. Combined with a shallow (75 km depth) low-velocity anomaly beneath 50°28′E, *Sauter et al.* [2009] interpreted that such a melt supply anomaly relates to the interaction between the SWIR and Crozet hotspot. Nonetheless, despite such strong geophysical evidence for possible plume-ridge interaction, critical geochemical evidence is missing as no E-MORB have been found along the ridge segments [*Gautheron et al.*, 2015; *Mahoney et al.*, 1992; *Meyzen et al.*, 2005]. Traditionally, interaction with the Crozet hotspot should produce E-MORB on the SWIR with higher $^{87}Sr/^{86}Sr$, $^{206}Pb/^{204}Pb$, $^{207}Pb/^{204}Pb$, and $^{208}Pb/^{204}Pb$ ratios and lower $^{143}Nd/^{144}Nd$ ratio and $^{176}Hf/^{177}Hf$ ratios than N-MORB [*Breton et al.*, 2013], but these were not previously reported. The majority of the MORB in the IFZ-GFZ section are N-MORB with depleted isotopic compositions. Only to the west of the IFZ (~45°45′E), E-MORB with Sr, Nd, Pb, and Hf isotopic anomalies were identified [*Janney et al.*, 2005; *Mahoney et al.*, 1992] and then inferred to be evidence of the interaction between the Crozet hotspot and SWIR [*Breton et al.*, 2013]. However, these E-MORB have isotopic compositions distinct from the Crozet hotspot (Figure 6) [*Janney et al.*, 2005; *Mahoney et al.*, 1992].

Only 13 MORB samples from the IFZ-GFZ section had been previously analyzed for Sr-Nd-Pb-(Hf) isotopic compositions so far. No such isotopic data are available for MORB from segment 27 with the anomalously thick crust up to 10 km. Thus, such a limited sample set could hardly reflect the actual geochemical variations of MORB erupted at the IFZ-GFZ section. R/V *Dayang Yihao* Cruise conducted intensive sampling at the IFZ-GFZ section during the past few years, and a group of N-MORB with enriched isotopic compositions was collected at segment 27. These samples provide critical constraints on the formation of such ultrathick crust on an ultraslow-spreading ridge, and possible interaction between the Crozet hotspot and SWIR. Combined with global distributions of isotopically enriched N-MORB, we propose that isotopically enriched N-MORB can be an indicator of off-axis plume-ridge interactions.

2. Geological Background

The SWIR is among the world's slowest-spreading ridges, with an almost constant full spreading rate of ~14 mm/yr between the Prince Edward Fracture Zone (35°E, Figure 1a) and its eastern end at 70°E [*Horner-Johnson et al*., 2005]. Bathymetric data revealed a shallow central region between the Prince Edward and Gallieni Fracture Zones (52°20′E), with an average depth of ~3200 m relative to the deeper western (~4000 m) and easternmost (~4500 m) portions of the ridge (Figure 1a) [*Cannat et al*., 2008; *Sauter et al*., 2001]. Such a bathymetric high is also correlated with low MBA and low Na_8 (Na_2O contents corrected for fractional crystallization at MgO = 8 wt % [*Klein and Langmuir*, 1987]) of the MORB in this region [*Cannat et al*., 2008]. All of these were previously interpreted as evidence for thicker crust and a higher degree of partial melting of a hotter mantle [*Cannat et al*., 1999, 2008]. Nonetheless, extensive exposures of mantle peridotites have led *Zhou and Dick* [2013] to argue for a generally thin and often missing crust and to suggest that the shallow bathymetry is due to an isostatic compensation of low-density depleted mantle.

Ridge segments between the Indomed (46°E) and Gallieni FZs, in the central shallow portion of the SWIR, are characterized by axial rifts over almost the entire section except for segment 27. They have an overall 15° obliquity and are devoid of transform faults, with nontransform discontinuities (NTDs) between ridge segments. Anomalously shallow ridge flanks were interpreted to indicate a dramatic increase in magma supply since 8–10 Ma [*Sauter et al*., 2004, 2001] and that it is characterized by robust magmatism with abundant basalts at the seabed [*Sauter et al*., 2004], and without peridotites [*Zhou and Dick*, 2013]. The only axial high exists along segment 27 (~50°28′E), a 72 km long segment where the axial depth is on average 1000 m shallower than nearby ridge segments (Figure 3a) and numerous volcanic edifices are present on both flanks of the axial valley, with relatively flat topography to the north and greater relief to the south (Figure 1b) [*Niu et al*., 2015]. Segment 27 shows a pronounced MBA low and a large negative anomalies of *S* wave velocities at depth [*Sauter et al*., 2001], with anomalously thick crust of up to 10 km at the segment center [*Niu et al*., 2015] and off axis within a 20 km distance [*Li et al*., 2015]. The thick oceanic crust indicates robust magma supply in this area, which has been inferred to be associated with the Crozet hotspot [*Sauter et al*., 2009; *Zhang et al*., 2013]. An inactive hydrothermal vent is located in the center of segment 27 and an active hydrothermal vent field is located near the oceanic core complex on the southern flank [*Zhao et al*., 2013] of the segment 28 [*Tao et al*., 2012].

There are several oceanic plateaus including the Marion Plateau, the Del Cano Rise, and the Crozet Plateau (Figure 1a). The Crozet Plateau located ~900 km south of the IFZ-GFZ section, in particular, is composed of five islands and islets dated from 8.75 to 0.1 Ma [*Cantagrel et al*., 1980] lying on a 54 Ma basaltic plateau [*Goslin et al*., 1981], which can be geographically divided into western and eastern islands separated by the 2 km deep N-S trending basin as described in detail in *Breton et al*. [2013] (Figure 1a).

3. Sampling and Petrography

Samples in this study were collected along the axis of the SWIR during the R/V *Dayang Yihao* cruises DY105-17, DY115-19, DY115-20, and DY115-21, mostly via TV grab (TVG) and only a few by dredging. Forty-seven samples are from the IFZ-GFZ section including 15 samples from segment 27 (Figure 1).

MORB collected from the IFZ-GFZ section are mostly whole-rock samples with fine-grained and slightly phyric textures. They contain <5 vol % phenocrysts of euhedral olivine, mostly skeletal plagioclase, and minor Cr-spinel near or included in olivine crystals. Variolitic to intersertal matrix varies from glassy quenched rims to more holocrystalline interiors and is composed of microcrystals of plagioclase, and clinopyroxene and

Table 1. Major and Trace Elemental Compositions of MORB From Segment 27, Southwest Indian Ridge[a]

Sample	21VI-14-8	21VI-11-7	SW-V-6	SW-III-8-1	SW-III-8-2	SW-III-9	20V-11-3	SW-III-11-1	SW-III-11-2	SW-III-12	SW-IV-7	SW-III-22	SW-III-14-1	SW-III-14-2	SW-III-15
Type	Main	Main	Main	Main	Main	Main	Main	High-Al	High-Al	High-Al	High-Al	High-Al	High-Al	High-Al	High-Al
Longitude (°E)	50.47	50.47	50.47	50.47	50.47	50.47	50.47	50.47	50.47	50.47	50.47	50.47	50.46	50.46	50.46
Latitude (°S)	37.68	37.68	37.68	37.66	37.66	37.66	37.66	37.66	37.66	37.66	37.66	37.66	37.65	37.65	37.65
Depth (m)	1640	1719	1631	1751	1751	1751	1764	1751	1751	1776	1725	1725	1729	1729	1729
								Oxides (wt %)							
SiO_2	50.23	50.26	50.15	49.78	49.75	49.77	50.22	47.75	47.78	47.84	47.55	47.69	48.29	47.95	48.56
TiO_2	1.39	1.40	1.34	1.35	1.35	1.37	1.33	0.82	0.82	0.84	0.85	0.80	0.92	0.87	0.93
Al_2O_3	15.04	15.00	14.86	14.89	14.82	14.81	14.87	16.71	16.87	16.21	17.07	17.41	16.56	15.62	16.49
Fe_2O_3	11.07	10.99	10.95	11.95	11.96	12.01	10.90	10.91	10.89	11.11	10.73	10.79	11.20	11.16	10.99
MnO	0.18	0.18	0.17	0.17	0.18	0.18	0.17	0.14	0.14	0.14	0.15	0.13	0.15	0.14	0.14
MgO	7.44	7.56	7.49	7.77	7.78	7.71	7.76	9.11	8.78	9.68	8.90	8.34	7.89	10.40	8.14
CaO	11.23	11.21	11.47	11.11	11.19	11.23	11.40	11.29	11.42	11.21	11.62	11.71	11.56	10.89	11.41
Na_2O	2.60	2.55	2.59	2.65	2.59	2.55	2.60	2.86	2.62	2.48	2.43	2.72	2.65	2.46	2.62
K_2O	0.16	0.22	0.21	0.08	0.09	0.09	0.22	0.11	0.13	0.14	0.07	0.08	0.20	0.16	0.23
P_2O_5	0.09	0.09	0.09	0.06	0.06	0.06	0.10	0.06		0.00	0.06	0.01	0.00		
L.O.I.	0.05	0.05	0.18	−0.27	−0.24	−0.25	−0.08	−0.24	0.07	−0.15	0.01	−0.20	0.08	−0.12	−0.01
Total	99.50	99.50	99.50	99.53	99.52	99.52	99.50	99.52	99.50	99.50	99.41	99.49	99.50	99.52	99.50
Na_8	2.49	2.48	2.49	2.64	2.59	2.53	2.60	2.95	2.69	2.59	2.50	2.93	2.71	2.62	2.77
Mg#	61	62	61	60	60	60	62	66	65	67	66	64	62	68	63
								Trace Elements (ppm)							
Sc	43.8	41.8	43.7	41.9	38.8	40.9	41.1	32.6	33.2	30.9	32.5	32.0	34.3	32.2	33.9
V	323	314	326	312	296	314	306	184	185	175	194	179	203	191	203
Cr	213	212	205	214	210	216	208	351	329	403	274	289	299	494	333
Ni	89.7	91.7	87.4	106	105	102	91.5	174	172	214	151	158	130	275	158
Cu	82.5	76.4	71.8	89.8	80.7	85.5	49.2	84.2	90.2	82.9	70.9	88.8	97.1	93.4	102
Rb	1.54	1.99	1.47	0.686	0.668	0.646	1.50	1.13	2.43	2.08	0.528	1.09	3.26	2.60	4.19
Sr	105	106	108	83.7	84.9	83.8	105	114	121	108	188	120	115	110	114
Y	29.5	29.9	30.0	32.1	30.7	33.1	30.2	17.6	18.0	17.1	16.7	16.9	19.5	18.2	19.6
Zr	83.5	83.3	84.3	79.2	78.4	76.4	84.1	43.5	44.8	44.5	45.9	43.2	47.7	45.9	47.9
Nb	1.01	1.01	1.02	1.00	1.05	0.977	1.03	0.600	0.639	0.611	0.581	0.710	0.666	0.679	0.713
Ba	7.31	6.79	7.76	6.80	8.00	7.10	7.17	4.36	4.25	3.34	4.96	3.21	4.24	5.80	4.02
La	1.78	1.80	1.74	2.05	2.21	2.12	1.81	1.42	1.47	1.50	1.46	1.36	1.63	1.52	1.62
Ce	6.22	6.38	6.14	6.95	8.34	7.40	6.43	4.74	4.61	4.86	4.70	4.42	5.06	4.73	5.02
Pr	1.21	1.25	1.20	1.36	1.54	1.39	1.27	0.866	0.863	0.919	0.872	0.871	1.11	0.904	0.947
Nd	7.03	7.32	7.07	8.01	8.63	8.20	7.33	4.74	4.85	4.96	4.61	4.69	5.39	4.98	5.21
Sm	2.85	2.96	2.85	3.12	3.32	3.17	3.01	1.75	1.83	1.79	1.69	1.69	1.99	1.88	1.97
Eu	1.13	1.15	1.09	1.15	1.20	1.18	1.13	0.732	0.748	0.753	0.691	0.756	0.838	0.790	0.830
Gd	4.18	4.31	4.25	4.56	4.85	4.66	4.35	2.43	2.61	2.63	2.28	2.44	2.88	2.75	2.89
Tb	0.784	0.831	0.796	0.900	0.940	0.910	0.822	0.504	0.506	0.502	0.461	0.478	0.574	0.527	0.577
Dy	5.46	5.72	5.61	5.64	6.00	6.00	5.64	3.24	3.27	3.42	3.12	3.17	3.61	3.42	3.55
Ho	1.18	1.26	1.22	1.27	1.33	1.32	1.23	0.731	0.739	0.742	0.670	0.702	0.826	0.760	0.813
Er	3.33	3.48	3.42	3.63	3.82	3.64	3.46	2.04	2.08	2.06	1.88	2.00	2.27	2.05	2.21
Tm	0.519	0.533	0.521	0.540	0.568	0.531	0.536	0.301	0.312	0.303	0.275	0.285	0.336	0.294	0.318
Yb	3.24	3.43	3.33	3.46	3.53	3.50	3.45	1.94	1.96	1.89	1.76	1.84	2.14	2.00	2.09
Lu	0.494	0.532	0.504	0.524	0.560	0.540	0.516	0.298	0.296	0.293	0.278	0.288	0.320	0.298	0.311
Hf	2.20	2.32	2.27	2.30	2.35	2.39	2.31	1.27	1.27	1.25	1.20	1.12	1.38	1.34	1.40
Ta	0.089	0.089	0.086	0.125	0.145	0.115	0.088	0.084	0.083	0.090	0.063	0.050	0.080	0.084	0.093
Th	0.084	0.066	0.072	0.087	0.168	0.113	0.066	0.058	0.063	0.085	0.041	0.049	0.065	0.072	0.097

AGU Journal of Geophysical Research: Solid Earth

10.1002/2016JB013284

AGU Journal of Geophysical Research: Solid Earth

10.1002/2016JB013284

Table 1. (continued)

Element Ratios															
$(La/Sm)_N$	0.39	0.38	0.39	0.41	0.42	0.42	0.38	0.51	0.50	0.52	0.54	0.51	0.51	0.51	0.51
$(Sr/Nd)_N$	0.96	0.93	0.98	0.67	0.63	0.66	0.92	1.55	1.61	1.41	2.63	1.65	1.37	1.42	1.40
$(La/Yb)_N$	0.39	0.38	0.37	0.43	0.45	0.43	0.38	0.53	0.54	0.57	0.60	0.53	0.54	0.55	0.56

[a]Na_8: Na_2O contents corrected for fractional crystallization at MgO = 8 wt % [*Klein and Langmuir*, 1987]. The correction methods used are from *Klein and Langmuir* [1987] for MORB with MgO < 8.5 wt %, and from *Klein et al*. [1991] for MORB with MgO > 8.5 wt %.

Table 2. Isotopic Compositions of MORB From 46 to 52°E SWIR

Sample	Segment	Latitude (°S)	Longitude (°E)	$^{87}Sr/^{86}Sr$	$\pm 2\sigma$	$^{143}Nd/^{144}Nd$	$\pm 2\sigma$	$^{176}Hf/^{177}Hf$	$\pm 2\sigma$	$^{206}Pb/^{204}Pb$	$^{207}Pb/^{204}Pb$	$^{208}Pb/^{204}Pb$
Main MORB												
SW-V-4	30	38.13	48.6	0.703071	0.000010	0.513124	0.000006	0.283254	0.000005	18.276	15.533	38.163
21VII-34-21	29	37.91	49.25	0.702935	0.000014	0.513098	0.000011	0.283203	0.000008	18.188	15.535	38.107
IR-2	28	37.77	49.65	0.702978	0.000011	0.513118	0.000008	0.283225	0.000006	18.277	15.564	38.248
21 V-3-1	28	37.78	49.65	0.702950	0.000010	0.513123	0.000004			18.221	15.528	38.117
SW-9-A	28	37.78	49.65	0.702924	0.000013	0.513117	0.000007	0.283228	0.000006	17.99	15.528	37.807
21 V-29-6	28	37.78	49.65	0.702983	0.000013	0.513133	0.000004			18.212	15.53	38.128
21VI-11-7	27	37.68	50.47	0.702869	0.000016	0.513140	0.000006	0.283221	0.000008	18.202	15.526	38.094
21VI-14-8	27	37.68	50.47	0.702830	0.000014	0.513135	0.000005	0.283225	0.000008	18.164	15.531	38.097
SW-III-18	26	37.61	50.97	0.702969	0.000011	0.513132	0.000008	0.283237	0.000005	18.216	15.55	38.169
SW-III-21	25	37.47	51.72			0.513111	0.000003	0.283235	0.000003			
High-Al MORB												
SW-IV-7	27	37.66	50.47	0.703343	0.000010	0.512997	0.000014	0.283101	0.000008			
SW-III-11-1	27	37.66	50.47	0.703377	0.000009	0.512989	0.000008	0.283106	0.000006			
SW-III-11-2	27	37.66	50.47	0.703376	0.000009	0.512984	0.000008	0.283098	0.000005			
SW-III-12	27	37.66	50.47	0.703307	0.000012	0.513002	0.000007	0.283111	0.000005	18.586	15.57	38.601
SW-III-14-1	27	37.65	50.46	0.703356	0.000011	0.512983	0.000009	0.283107	0.000006			
SW-III-14-1 (duplicate)				0.703341	0.000010	0.512996	0.000008					
SW-III-14-2	27	37.66	50.47	0.703350	0.000009	0.512990	0.000012	0.283083	0.000007			
SW-III-22	27	37.65	50.46	0.703313	0.000012	0.513002	0.000008	0.283120	0.000007			

glass. In general, samples are relatively fresh and contain few or no secondary minerals. Only a few samples contain minor iddingsite in the matrix or around the margins of olivine grains.

4. Analytical Methods

Interiors of pillows and glass samples were powdered to 200 mesh for major and trace elemental analyses. Powdered samples were then leached twice in 6 mol/L HCl for 60 min at 100°C, followed by ultrasonic leaching in Milli-Q water three times for Sr-Nd-Hf-Pb isotopic analyses.

Both major and trace element analyses were performed in Guangzhou Institute of Geochemistry, Chinese Academy of Sciences. Major elements were analyzed by X-ray fluorescence spectrometry, and the trace elements by inductively coupled plasma–mass spectrometry. Analytical uncertainties are ±1–2% for major elements, ±5% for rare earth elements, and ±5–10% for other trace elements. Detailed analytical procedures were given in *Li et al*. [2006] and *Liu et al*. [1996].

Sr-Nd-Hf isotopic compositions were obtained using a Neptune Plus multicollector mass spectrometer at Guangzhou Institute of Geochemistry, Chinese Academy of Sciences. Pb isotopic compositions were obtained using a thermal ionization mass spectrometry (TIMS) in the University of Science and Technology of China.

Sr, Nd, and Hf isotopic fractionations were corrected to $^{86}Sr/^{88}Sr = 0.1194$, $^{146}Nd/^{144}Nd = 0.7219$, and $^{179}Hf/^{177}Hf = 0.7325$, respectively. During the period of analyses, measured isotopes of NBS987, JNdi-1, and JMC475 standard materials are $^{87}Sr/^{86}Sr = 0.710265 \pm 0.000016$ (2σ, $n = 16$), $^{143}Nd/^{144}Nd = 0.512089 \pm 0.000013$ (2σ, $n = 18$), and $^{176}Hf/^{177}Hf = 0.282152 \pm 0.000010$ (2σ, $n = 11$), respectively. Total procedural blanks are <1 ng for Sr and <60 pg for Nd and Hf. To facilitate comparison, all sample data have been normalized to the NBS987, Jndi-1, and JMC 475 values of 0.71025, 0.512115, and 0.28216 for $^{87}Sr/^{86}Sr$, $^{143}Nd/^{144}Nd$, and $^{176}Hf/^{177}Hf$, respectively. Common lead standard NBS 981 yielded average values of $^{206}Pb/^{204}Pb = 16.943 \pm 0.002$ (2σ, $n = 12$), $^{207}Pb/^{204}Pb = 15.499 \pm 0.002$ (2σ, $n = 12$), and $^{208}Pb/^{204}Pb = 36.724 \pm 0.008$ (2σ, $n = 12$). All Pb data have been normalized to the NBS981 values of *Baker et al*. [2004]: 16.9418, 15.5000, and 36.7265 for $^{206}Pb/^{204}Pb$, $^{207}Pb/^{204}Pb$, and $^{208}Pb/^{204}Pb$, respectively. Total procedural Pb blanks were lower than 1 ng. The reproducibility is better than 0.01%. Measurements of standard materials, BCR-2 and BHVO-2, which were subject to the same chemical procedure as the MORB samples yielded isotopic ratios in agreement with U.S. Geological Survey recommended values and published values from GeoRem [e.g., *Weis et al*., 2007, 2006; *Woodhead and Hergt*, 2000] (BCR-2: $^{87}Sr/^{86}Sr = 0.705042 \pm 0.0000016(2\sigma)$, $^{143}Nd/^{144}Nd = 0.512629 \pm 0.000006(2\sigma)$, $^{176}Hf/^{177}Hf = 0.282858 \pm 0.000006(2\sigma)$, $^{206}Pb/^{204}Pb = 18.753$, $^{207}Pb/^{204}Pb = 15.614$ and $^{208}Pb/^{204}Pb = 38.699$; BHVO-2: $^{87}Sr/^{86}Sr = 0.703514 \pm 0.000010(2\sigma)$, $^{143}Nd/^{144}Nd = 0.512989 \pm 0.000008(2\sigma)$, and $^{176}Hf/^{177}Hf = 0.283084 \pm 0.000005(2\sigma)$). Duplicated sample of BCR-2 also yielded consistent results with $^{87}Sr/^{86}Sr$ ratios of $0.705050 \pm 0.000012(2\sigma)$, $^{143}Nd/^{144}Nd$ ratios of $0.512633 \pm 0.000007(2\sigma)$, and $^{176}Hf/^{177}Hf$ ratios of $0.282852 \pm 0.000005(2\sigma)$. Detailed analytical procedures for Sr, Nd, and Hf and Pb isotopic measurements are as described in *Wei et al*. [2002], *Li et al*. [2004], and *Chernyshev et al*. [2007], respectively.

5. Analytical Results

Major and trace elemental compositions for MORB from segment 27 and Sr-Nd-Hf-Pb isotopic compositions for all samples in this study are shown in Tables 1 and 2, respectively. Major and trace elemental compositions for all MORB in this study can be found in the supporting information (Data Set S1). We report 47 new major and trace elemental analyses from the IFZ-GFZ section, including 15 samples from segment 27.

5.1. Major Elements

Major elemental data for MORB from the IFZ-GFZ section cover a range of compositions from 7.44 to 10.4 wt % MgO. In particular, two groups of MORB from the IFZ-GFZ section are noteworthy.

1. The high-Al group from segment 27 has high Al_2O_3 (15.62–17.41 wt %) and MgO (7.89–10.4 wt %), and low SiO_2 (48.56–47.55 wt %) and TiO_2 (0.8–0.93 wt %). These basalts have characteristics similar to the high-Al basalts found along the Galápagos spreading center [*Eason and Sinton*, 2006] and FAMOUS

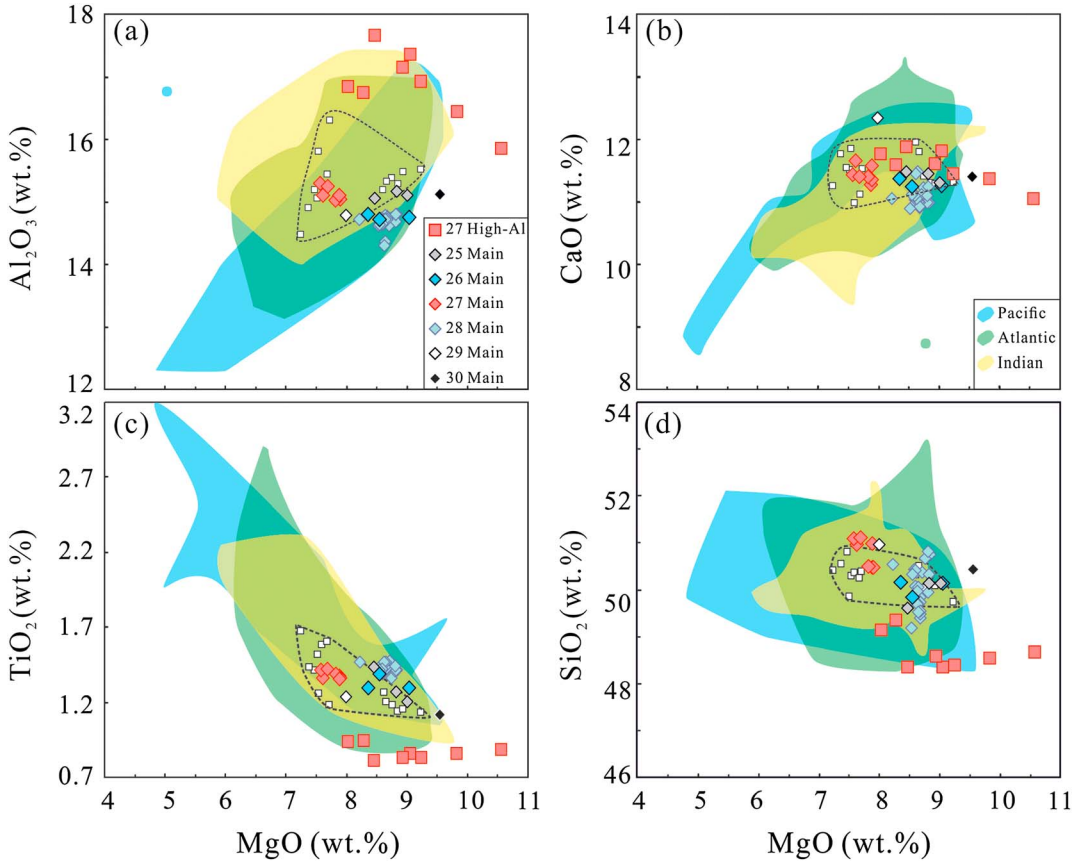

Figure 2. (a) MgO versus Al_2O_3, (b) MgO versus CaO, (c) MgO versus TiO_2, and (d) MgO versus SiO_2 plots of samples from the IFZ-GFZ section. Dashed fields are for 14 published data for MORB from the IFZ-GFZ (open squares) from PetDB [*Lehnert et al.*, 2000]. Blue, green, and yellow fields are for segment averages of Pacific, Atlantic, and Indian MOR, respectively [*Gale et al.*, 2013a]. All major elemental data have been normalized to a total of 100 wt % to facilitate comparison.

(French-American Mid-Ocean Undersea Study segment) [*Gale et al.*, 2013b]. No such samples have been identified from the IFZ-GFZ section before (Figure 2).

2. The dominant group of the IFZ-GFZ section (hereafter referred to as "Main") has MgO between 7.44 and 9.33 wt %, with lower Al_2O_3 (14.18–15.04 wt %), and higher TiO_2 (1.09–1.46 wt %) and SiO_2 (48.55–50.26 wt %) than the high-Al group. Their compositions are generally consistent with those published before from the same region (Figure 2).

Particularly, the high-Al MORB have only been collected from the center of segment 27 (50°28′E), along with the Main MORB at the same location (Figure 3). The Main samples from segment 27, with MgO from 7.44 to 7.78 wt %, are the most evolved MORB among the whole Main group. MORB from the IFZ-GFZ section show generally negative correlations between MgO and Al_2O_3 (Figure 2a), suggesting that plagioclase is not a major liquidus phase. High-Al MORB and Main MORB follow parallel evolution trends in the major element correlations (Figure 2).

5.2. Trace Elements

MORB from the IFZ-GFZ section are all typical N-MORB with chondrite-normalized $(La/Sm)_N$ lower than 0.7. Although all REE patterns are generally parallel, the high-Al samples have much lower REE contents than the Main group, particularly for heavy REE (Figure 4a). The high-Al samples are generally depleted in most incompatible elements but show positive Sr anomalies on the trace element spider diagrams (Figure 4b) compared to the Main group and have higher $(Sr/Nd)_N$ ratios (1.37–2.63). The High-Al MORB also have slightly higher $(La/Sm)_N$ (0.52–0.56) and $(La/Yb)_N$ (0.53–0.6) ratios than the Main MORB from the segment 27 (0.39–0.43 and 0.37–0.45, respectively), but comparable $(Sm/Yb)_N$ ratios (~1). Trace element variations of the high-Al MORB

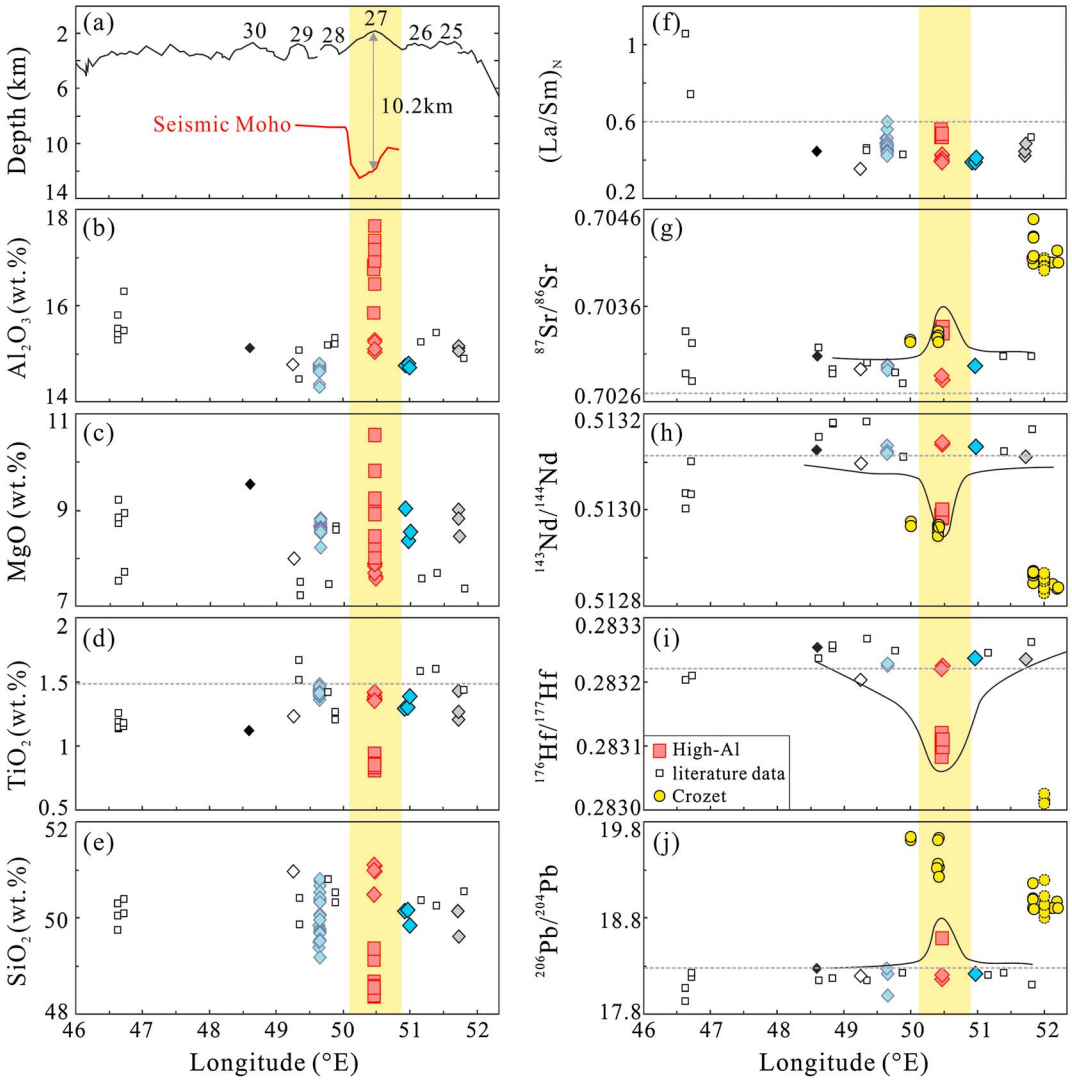

Figure 3. (a–j) Along-axis depth and chemical variations of MORB from the IFZ-GFZ. Diamonds are for Main MORB from different segments, the same as in Figure 2. The axial depths as well as depths of seismic Moho (red curve) and estimated crustal thickness (10.2 km for the center of segment 27) in Figure 3a are from *Mendel et al.* [2003] and *Niu et al.* [2015], respectively. Yellow fields mark segment 27 with both geophysical and geochemical anomalies. Dashed yellow dots are for Crozet samples without accurate locations from *Salters and White* [1998] and *Mahoney et al.* [1996]. Other data for Crozet samples are from *Breton et al.* [2013]. Dashed horizontal lines represent D-MORB arithmetic averages calculated with the data from *Gale et al.* [2013a]. Literature data (small squares) are from PetDB. Dark curves show the enriched isotopic characteristics of high-Al MORB from segment 27 compared with Main MORB and D-MORB averages.

and Main MORB show parallel evolution trends similar to the major element data (Figure S1). The Main MORB show generally positive correlations in the La versus $(La/Sm)_N$ diagram (Figure 5), whereas the high-Al MORB shift to lower La contents but higher $(La/Sm)_N$ ratios than the Main MORB from segment 27 (Figure 5).

5.3. Isotopes

The high-Al MORB from segment 27 have uniformly more enriched isotopic compositions with very limited variations ($^{87}Sr/^{86}Sr$: 0.703307–0.703377; $^{143}Nd/^{144}Nd$: 0.512983–0.513002; $^{176}Hf/^{177}Hf$: 0.283083–0.283120; $^{206}Pb/^{204}Pb$: 18.586; $^{207}Pb/^{204}Pb$: 15.570; and $^{208}Pb/^{204}Pb$: 38.601) than the Main MORB from the IFZ-GFZ section ($^{87}Sr/^{86}Sr$: 0.702830–0.703071; $^{143}Nd/^{144}Nd$: 0.513098–0.513140; $^{176}Hf/^{177}Hf$: 0.283225–0.283254; $^{206}Pb/^{204}Pb$: 17.990–18.277; $^{207}Pb/^{204}Pb$: 15.526–15.564; and $^{208}Pb/^{204}Pb$: 37.807–38.248) (Figures 3 and 6). Sr-Nd-Hf-Pb isotopes of the samples show relatively good correlations with one another (Figure 6). In

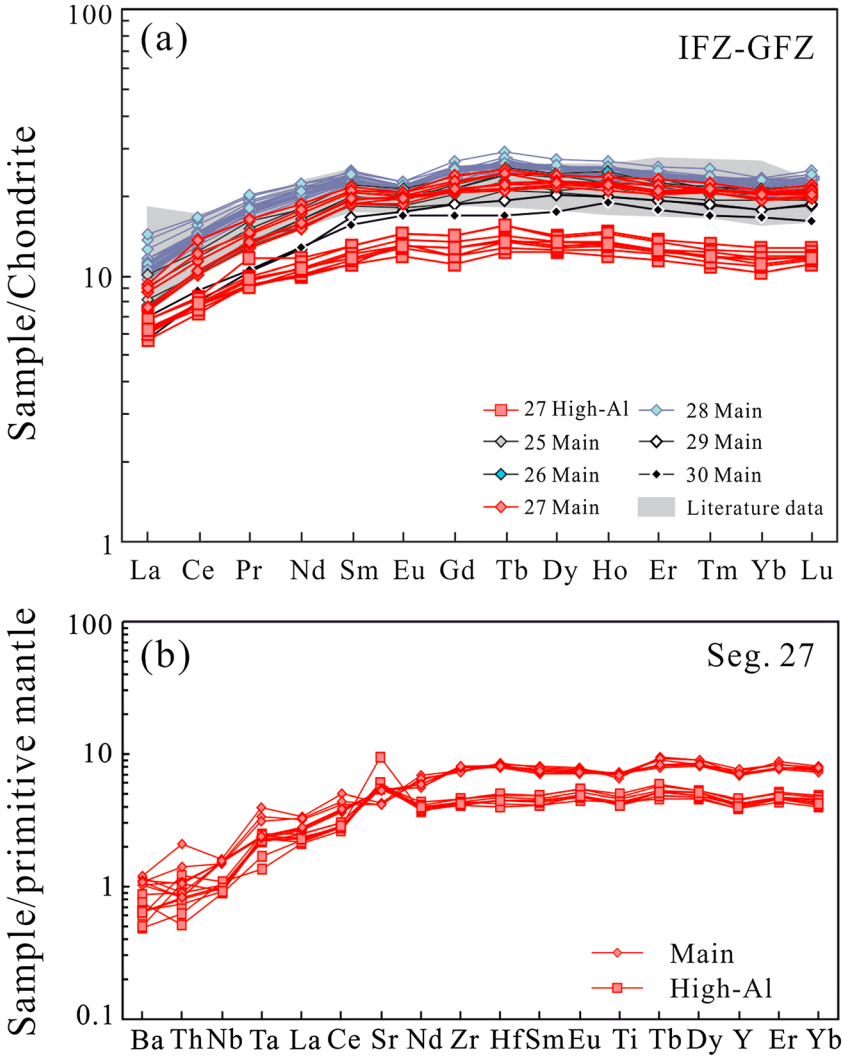

Figure 4. (a) REE patterns of the basalts from the IFZ-GFZ section. The shadow field shows the literature REE data of six MORB samples from this region. High-Al N-MORB have distinctly lower REE than Main MORB from the IFZ-GFZ. Chondrite data are from *Sun and McDonough* [1989]. Literature data are from PetDB. (b) Trace element spider diagrams of basalts from segment 27. High-Al N-MORB show positive Sr anomalies. Primitive mantle data are from *McDonough and Sun* [1995].

particular, the high-Al MORB have more depleted elemental compositions but enriched isotopic compositions compared with global MORB average from *Gale et al.* [2013a], plotted far off the commonly coupled enrichment/depletion trends of trace elements and isotopes defined by both global MORB averages and MORB from ridge segments within 200 km of a hotspot (Figure 7).

6. Discussion

At ultraslow-spreading ridges, it is widely acknowledged that because of decreased mantle upwelling, the lithosphere is thicker, leading to a shorter melting column and a decreased total volume of melt production [*Bown and White*, 1994]. As a result, crustal thickness drops off irregularly and dramatically [e.g., *Jokat et al.*, 2003; *Jokat and Schmid-Aursch*, 2007; *Reid and Jackson*, 1981]. Nonetheless, except for segment 27, anomalously thick crust has also been reported between 11°E and 15°E SWIR, the Joseph Mayes Seamount (10 km thick) and the Narrowgate segments (7.5 km thick), with amagmatic segments in between. These crustal thickness variations have been proposed to reflect the along-axis melt focusing from beneath amagmatic segments to the two magma-robust segments, controlled by the oblique spreading at ultraslow-spreading ridges [*Standish et al.*, 2008]. MORB erupted on the two magma-robust segments are mainly evolved

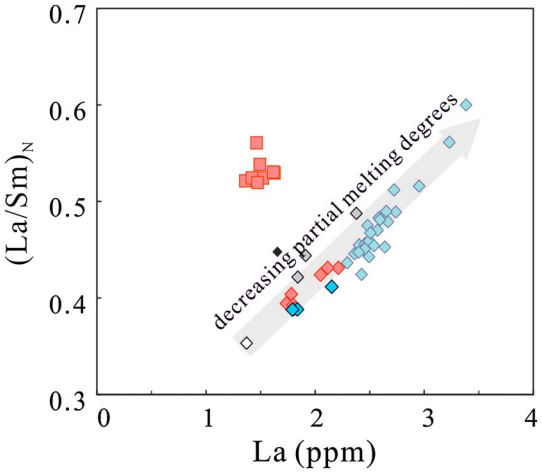

Figure 5. La versus $(La/Sm)_N$ plots of samples from the IFZ-GFZ section. Grey arrow indicates the trend for decreasing partial melting degrees.

E-MORB and were interpreted to result from melting of a pyroxenite-bearing heterogeneous source [*Standish et al*., 2008]. In this model, a more fusible pyroxenite in the source would produce a magma-robust segment. However, it is not the case for the accretion of segment 27, as E-MORB, which would indicate the presence of a fertile and fusible mantle source, have not been discovered so far. The occurrence of only N-MORB in segment 27, alternatively, indicates a generally depleted and refractory source, the melting of which would not be expected to produce thick crust under typical melting conditions. Therefore, the formation of ultrathick crust at segment 27 calls for other explanations.

Both the Main and high-Al MORB with distinct elemental and isotopic compositions erupted at the center of segment 27 with a 10 km thick crust.

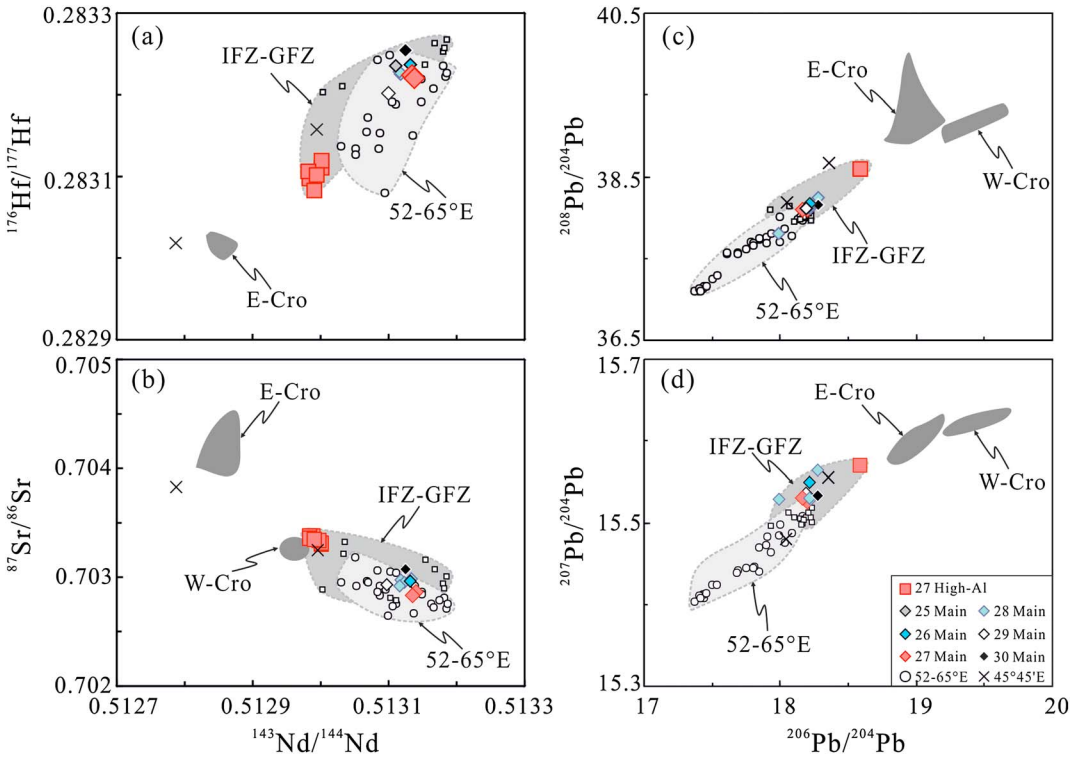

Figure 6. Sr, Nd, Hf, and Pb isotopic covariation diagrams for SWIR MORB. Grey shaded fields represent MORB data both in this study and in the literature from the IFZ-GFZ section and 52–65°E as noted. Published data for the two regions are shown as small squares and circles, respectively. Dark grey shaded fields are for basalt compositions from eastern (E-Cro) and western Crozet islands (W-Cro) [*Breton et al*., 2013; *Mahoney et al*., 1996; *Salters and White*, 1998]. Crosses are for E-MORB from 45°45′E, immediately west of the IFZ. All the previous published MORB data from the SWIR are from PetDB. All data have been normalized to the NBS987 and JMC 475 values of 0.71025 and 0.28216 for $^{87}Sr/^{86}Sr$ and $^{176}Hf/^{177}Hf$, respectively. Due to different standards used in the literature data for Nd analyses, $^{143}Nd/^{144}Nd$ data reported with standards Jndi-1 and La Jolla were normalized to 0.512115 and 0.511858, respectively, based on the correlation of analyzed data of the two standards [*Tanaka et al*., 2000]. Nd isotopic data reported with Johnson Matthey as standard are not used due to the large variations of published Nd ratios for the standard. Pb isotopic data have been normalized to the NBS981 values of *Baker et al*. [2004]: 16.9418, 15.5000, and 36.7265 for $^{206}Pb/^{204}Pb$, $^{207}Pb/^{204}Pb$, and $^{208}Pb/^{204}Pb$, respectively.

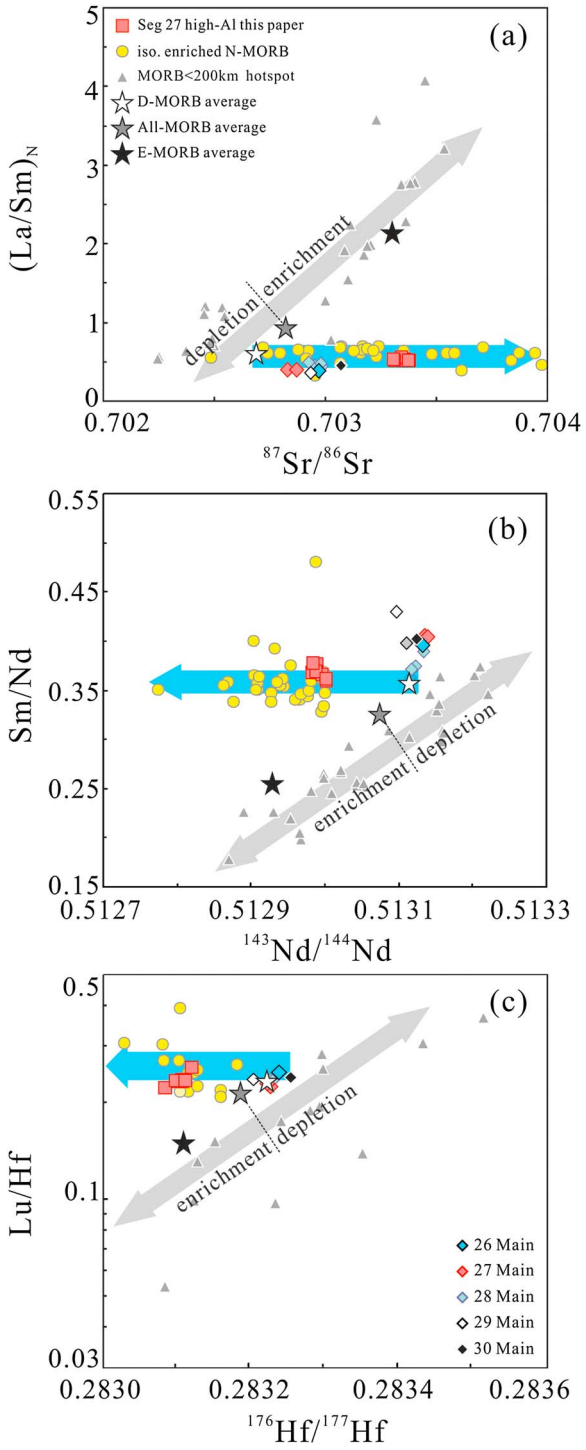

Figure 7. Plots of (a) $(La/Sm)_N$ versus $^{87}Sr/^{86}Sr$, (b) Sm/Nd versus $^{143}Nd/^{144}Nd$, and (c) Lu/Hf versus $^{176}Hf/^{177}Hf$ for MORB from the IFZ-GFZ section. Grey star represents the composition of average All-MORB estimates from *Gale et al.* [2013a]. White and black stars represent the arithmetic mean values of D-MORB and E-MORB calculated based on the classification and dataset of *Gale et al.* [2013a]. Grey arrows show the commonly coupled enrichment/depletion trends of both isotopes and trace elements for global MORB represented by the chemical variations of global MORB averages as well as MORB distributed within 200 km of hotspots (grey triangles). Blue arrows, on the other hand, show a totally different trend exhibiting decoupled isotopic and trace element enrichments, represented by high-Al MORB in this study and isotopically enriched N-MORB elsewhere (yellow circles; literature data are compiled in Data Set S2 in the supporting information). It is clearly demonstrated here that these samples have depleted trace elemental (lower $(La/Sm)_N$; higher Sm/Nd and Lu/Hf) but enriched isotopic compositions (higher $^{87}Sr/^{86}Sr$; lower $^{143}Nd/^{144}Nd$ and $^{176}Hf/^{177}Hf$) relative to the All-MORB average.

The former have comparable compositions with other Main MORB from the IFZ-GFZ section. The high-Al MORB, on the other hand, are unique in both elemental and isotopic compositions (Figures 2–6). In particular, they have depleted incompatible elemental but relatively enriched isotopic compositions, distinct from the commonly coupled enrichment/depletion of trace elements and isotopes for both global MORB and MORB from ridge segments within 200 km of a hotspot (Figure 7). These observations raise three major points that need to be addressed: (1) petrogenesis of the high-Al isotopically enriched N-MORB and their relationship with the interaction between the Crozet hotspot and SWIR; (2) segment-scale crustal accretion to form a 10 km thick crust along an ultraslow-spreading ridge; and (3) possible correlation of isotopically enriched N-MORB and off-axis plume-ridge interaction globally.

6.1. Origin of the Isotopically Enriched High-Al N-MORB

The high-Al MORB, with higher Al_2O_3 and MgO and lower SiO_2 and TiO_2 contents, have relatively enriched isotopic compositions but similarly depleted trace element compositions compared with the Main MORB (Figures 3 and 4). We suggest that these diverse characteristics are not caused by a single set of circumstances but that the major and trace elemental signatures have been modified by reaction processes in the crust, whereas the isotopic compositions preserve the mantle history.

The isotopic compositions of the high-Al MORB show very limited variations and do not change with fractionation index MgO (Tables 1 and 2), suggesting that the enriched isotopic feature is inherited from their mantle source. Therefore, the isotopic variations of the high-Al MORB and Main MORB (Figure 6) indicate that they originated from different primary magmas and their mantle sources have varied isotopic compositions. Despite isotopic variations, the two groups have similarly depleted trace elemental compositions in that they are both N-MORB with $(La/Sm)_N < 0.7$ with parallel REE patterns and spider diagrams except for Sr (Figure 4), which were usually interpreted to reflect different fractionation degrees of a single magma suite. Therefore, it could be inferred that the source of the high-Al MORB is isotopically more enriched than that for the Main MORB, but both sources are similarly depleted in trace elements. Thus, the Main MORB can be used as a reference to investigate the petrogenesis of high-Al MORB.

6.1.1. High-Al Feature: Melt-Rock Reaction

Al is a moderately incompatible element during partial melting; thus, lower partial melting degrees of mantle peridotite could produce magma with higher Al_2O_3 contents [*Gale et al*., 2014]. However, such an interpretation for the high-Al feature can be easily ruled out as it would also increase the magma in TiO_2 and incompatible elemental contents, inconsistent with the chemical compositions of the high-Al MORB (Figures 2, 4, and S1). In addition, the Main MORB show generally positive correlations in the La versus $(La/Sm)_N$ diagram (Figure 5), indicating that they may derive from different partial melting degrees of the same mantle source. The high-Al MORB, on the other hand, shift to lower La contents but slightly higher $(La/Sm)_N$ ratios (Figure 5), which would call for different explanations.

The high-Al MORB, characterized by exceptionally high Al_2O_3 contents, high MgO (mostly >8 wt %), low SiO_2 (e.g., 48 wt %), and often very low TiO_2, mostly occur at slow-spreading ridges or close to fracture zones and ridge terminations, particularly on the margins of hotspots [*Eason and Sinton*, 2006; *Gale et al*., 2014, 2013b; *Langmuir and Bender*, 1984; *Laubier et al*., 2012; *Melson and O'Hearn*, 1979; *Meyzen et al*., 2003; *Standish et al*., 2008]. However, high-Al MORB have not yet been reported to erupt on a magma-robust segment with a crust up to 10 km thick, suggesting that high-Al MORB at segment 27 might have different petrogenesis. Two main hypotheses have been suggested to explain the origin of the high-Al MORB: (1) *Eason and Sinton* [2006] attributed the presence of high-Al basalts in the Galápagos Spreading Center to high-pressure fractionation of clinopyroxene suppressing plagioclase fractionation and (2) high-Al basalts and/or melt inclusions were also proposed to result from the reaction between lower oceanic crust cumulates and migrating melt [*Danyushevsky et al*., 2004, 2003; *Gale et al*., 2013b; *Kamenetsky et al*., 1998; *Laubier et al*., 2012; *Lissenberg and Dick*, 2008; *Slater et al*., 2001].

To better discriminate these processes, the chemical consequences of both assimilation and high-pressure crystallization of a primitive magma are modeled (Figure 8). The primary melt composition of a Main MORB was chosen as the starting melt composition to show in general how different processes would influence magma evolution, but not to indicate any genetic relationship of Main MORB and high-Al MORB. We chose the Main MORB from segment 26 as they have higher Mg# and MgO than those from segment 27

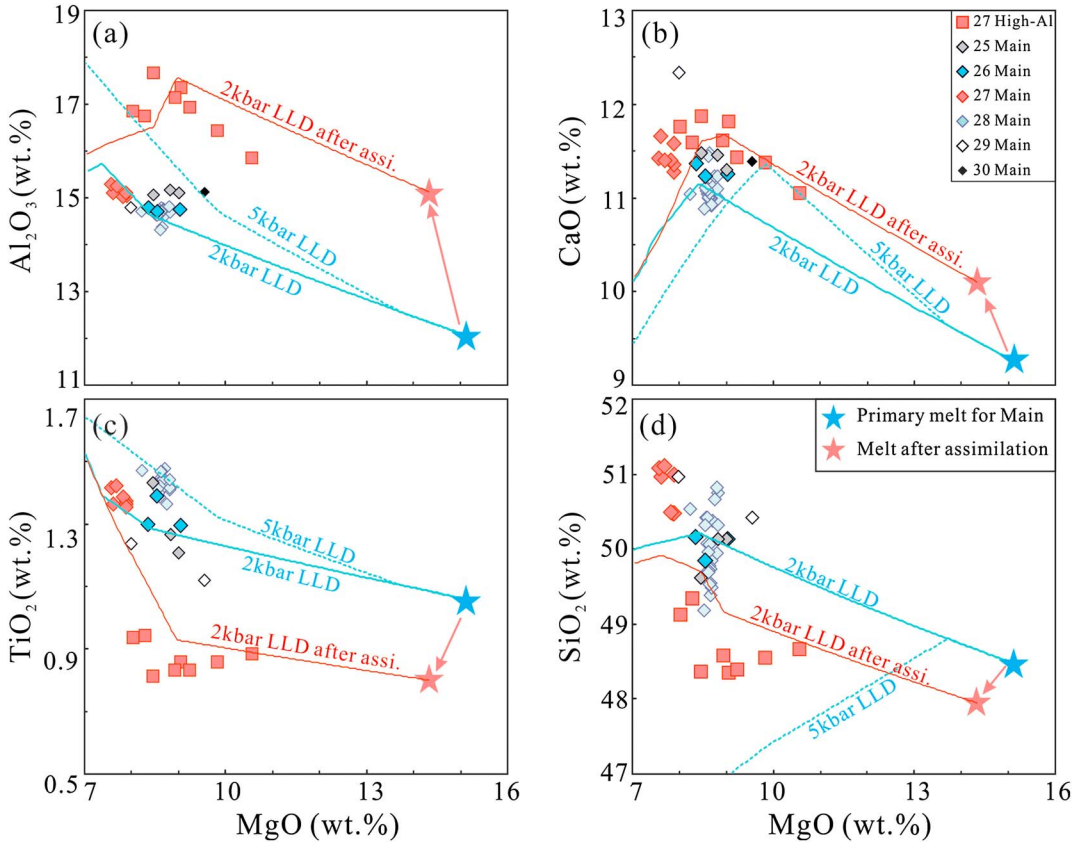

Figure 8. Major element modeling of the high-Al MORB via assimilation of a troctolite by a primary melt of Main MORB and subsequent crystallization at 2 kbar (red curves). The high- (5 kbar) and low-pressure (2 kbar) liquid lines of descent (LLD, blue curves) of the primary melt are also shown as comparison. The primary melt compositions of Main MORB used here are only considered as the reference for the high-Al MORB but do not indicate any genetic relationship with the high-Al MORB. The red curves represent 25% assimilation of olivine (Fo 88) + plagioclase (An 83) with plagioclase to olivine ratio of 3 by the primary melt. It is clear that assimilation of a primitive cumulate instead of high-P fractionation is more likely to produce the major elemental variations of the high-Al MORB, and also the 2 kbar LLD of the primary melt (blue curve) generally matches the major element variations of the Main MORB.

(Data Set S1). As plagioclase is not a major liquidus phase according to negative correlations between MgO and Al_2O_3 (Figure 2a), the primary melt compositions were estimated by adding incremental equilibrium olivine until the liquids were in equilibrium with mantle olivine (Fo 90). We added various amounts and proportions of plagioclase and olivine to this melt to model assimilation. Subsequent liquid lines of descent (LLD) of the assimilated melt at 2 kbar as well as the primary melt at 5 kbar (high pressure) and 2 kbar (low pressure) were modeled using MELTS [*Ghiorso and Sack*, 1995]. An example of the modeled assimilation of 25% olivine + plagioclase (plagioclase to olivine ratio of 3) and subsequent fractional crystallization is presented in Figure 8, together with LLDs at different pressures. It clearly shows that assimilation instead of high-P fractionation is more likely the process to produce the major elemental variations of the high-Al MORB (Figure 8). With varying assimilated amounts and phase ratios, our modeling all produce an increase in Al_2O_3, and decrease in SiO_2 and TiO_2, characteristics of high-Al MORB. Combining with similar calculation results of *Laubier et al.* [2012] for the origin of high-Al melt inclusions from the Mid-Atlantic Ridge, we infer that the reaction between MORB magma and primitive cumulates would all produce such chemical consequences independent of parental magma compositions.

High-Al MORB from segment 27 have generally lower incompatible elemental contents than the Main group, and they show positive Sr anomalies with $(Sr/Nd)_N$ higher than 1 (Figure 4). Consistently lower incompatible elements except for Ni and Sr compared to the Main MORB (Figures 4 and S1), accord with a dilution effect due to olivine and plagioclase assimilation, and lower Sc contents (Figure S1) also suggest that clinopyroxene

might not be a reacted phase, also consistent with the modeling. Thus, we propose that assimilation of the primitive cumulates (troctolite) could produce magma with the observed major and trace elemental compositions for the high-Al MORB from segment 27. Further evidence from experimental studies also suggests that basaltic magma would have higher Al_2O_3 and lower TiO_2 and SiO_2 after assimilation with olivine and plagioclase [*Yang et al*., 2015].

6.1.2. Enriched Isotopic but Depleted Elemental Compositions: Involvement of the Crozet HotSpot

Isotopic enrichment of MORB is often explained by the involvement of isotopically enriched materials in the source. But such enriched materials should also have enriched elemental compositions, resulting in E-MORB magmas. The lack of typical E-MORB at segment 27, however, argue against any local "fertile" mantle heterogeneity responsible for the anomalously thick crust at segment 27 as proposed by *Niu et al*. [2015]. Therefore, some particular geological processes are necessary to deplete the incompatible elements in the source to explain the isotopically enriched N-MORB (Figures 3 and 7). One possible scenario would be a recent melt extraction event of an originally enriched source. Under this circumstance, the enriched isotopic compositions could be preserved because the "recent" melting event would not significantly change the isotopic ratios in a short period due to relatively long half-time of the radioactive elements of Sm, Rb, Lu, U, and Th, but incompatible elements were largely depleted in the source to resemble the depleted mantle source for N-MORB (DMM). Thus, the likely "recent" melting events that might be related to the SWIR could be (1) Madagascar and Karoo flood basalt magmatism [*Zhou and Dick*, 2013] and (2) Crozet hotspot magmatism.

The extensive exposure of abyssal peridotites along the topographically high central SWIR with generally deep axial rifts was interpreted to be an isostatic response to the melting events to form the Karoo and Madagascar flood basalts [*Zhou and Dick*, 2013]. Such a depleted melting residue would likely have enriched isotopic and depleted trace elemental signatures, which could be the candidate for the source of the high-Al MORB from segment 27. However, in our study area the 1 km high and 72 km long axial volcano and anomalously thick crust both at the center and off axis revealed by geophysical studies [*Li et al*., 2015; *Niu et al*., 2015] all indicate robust magmatism beneath segment 27 in the past 3 Ma [*Li et al*., 2015] and even 10 Ma [*Sauter et al*., 2009]. Considering the refractory and cold nature of the plume residues after the melt extraction event some 100–200 Ma to form the Madagascar and Karoo flood basalts, it is highly unlikely that remelting such a residue could produce enough magma to form the oceanic crust at segment 27 with almost twice the thickness of nearby segments for the duration of at least 3 Ma. Such a cold mantle is also inconsistent with estimated higher mantle temperature beneath segment 27 with a large negative *S* wave anomaly [*Sauter et al*., 2009]. In fact, it would be hard for any potential originally enriched sources that had undergone melt extraction to remelt significantly to form such a magma-robust segment without a substantial heat source for such a long geologic time. Thus, neither the specific depleted Karoo and Madagascar flood basalt residues nor local mantle heterogeneity adequately explain the geochemical and geophysical observations at segment 27.

The volcanic activity of the Crozet hotspot, on the other hand, is recent, dated from 8.75 to 0.1 Ma [*Cantagrel et al*., 1980]; thus, the possible interaction of the hot plume with the ridge would provide enough heat to support robust magmatism to form the observed thick crust at segment 27. Such a plume-ridge interaction has been proposed by geophysical studies. A shallow (75 km depth) low-velocity anomaly, localized between the IFZ and GFZ (centered at segment 27), is found to be connected to a larger anomaly at the bottom of the lithosphere, which was interpreted to result from mantle outpouring of hot Crozet plume materials [*Sauter et al*., 2009]. It has been suggested that during lateral flow to the ridge axis, plume materials would undergo decompression melting off axis [*Hall and Kincaid*, 2003, 2004; *Sleep*, 1996], which would deplete the highly incompatible elements before they reach the ridge but would not change the isotopic compositions [*Hall and Kincaid*, 2003, 2004]. Thus, when the isotopically enriched but trace elemental depleted plume materials finally reach the ridge, further decompression melting at MOR would produce the isotopically enriched N-MORB at segment 27. The age of the volcanic activities of the Crozet hotspot are also consistent in time with enhanced melt supply for at least the past 3 Ma [*Li et al*., 2015].

To test such a plume-ridge interaction, MORB collected from the IFZ-GFZ section in this study were compared with those from ridge segments to the east of the IFZ-GFZ section (52–65°E) (Figure 6). It is clearly shown that MORB from segment 27 have more enriched Sr, Nd, Hf, and Pb isotopic signatures compared with MORB to the east. MORB from other segments in the IFZ-GFZ, on the other hand, show generally comparable isotopic compositions except for slight enrichment in Pb isotopes (Figure 6), which might be ascribed to Pb mobility

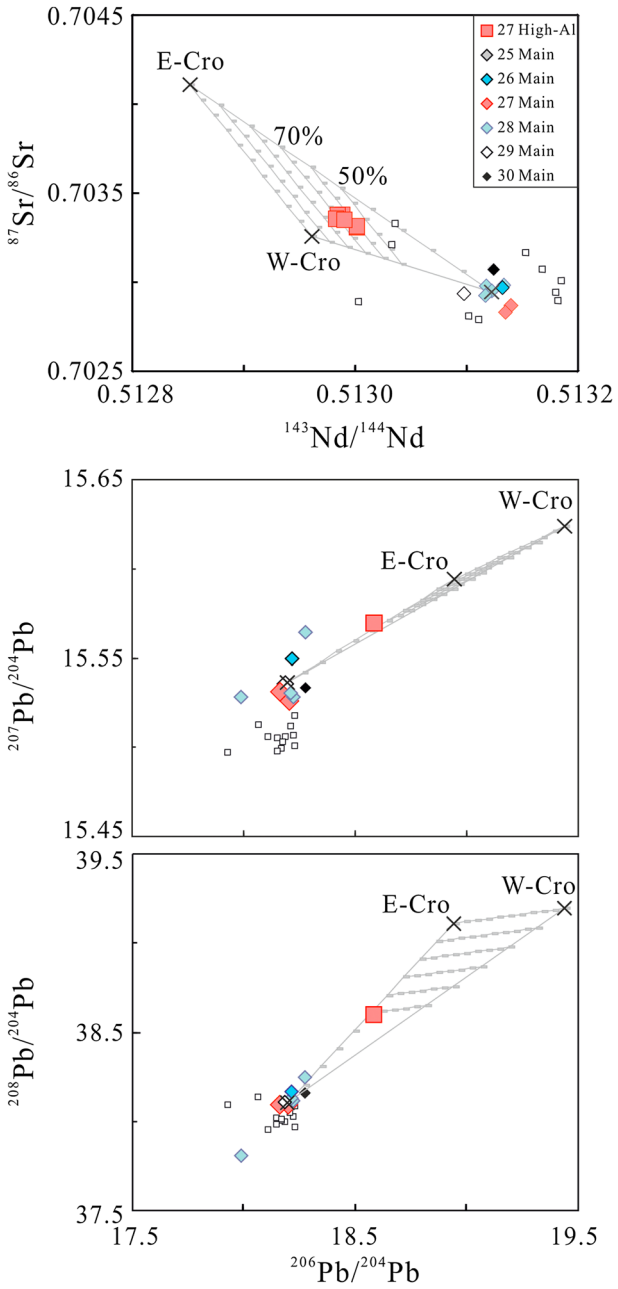

Figure 9. Quantitative modeling on the mantle source compositions of MORB from segment 27. The three modeling end-members are averages for Main MORB from segment 27 representing preexisting asthenospheric mantle compositions without the contribution of the Crozet hotspot, basalts from the western Crozet islands (W-Cro), and basalts from the eastern Crozet islands (E-Cro), respectively. Data sources are the same as in Figure 6. We used a simple 3-end-member mixing model based on the inference that the depleted melting residue of the Crozet hotspot end-members has similarly depleted trace elemental compositions as normal depleted mantle for N-MORB (DMM) as discussed in section 6.1. Marks on the modeled lines denote the relative percentage of mantle end-members (in 10% increments). Modeling suggests that the isotopically enriched N-MORB could be produced by melting of DMM mixed with 50%–70% Crozet plume materials with previous melt extraction. Hf isotopic variations are not modeled here due to the lack of Hf isotopic data of west Crozet plume.

during potential hydrothermal alteration as illustrated in the supplementary materials (Text S1 and Figure S2). Thus, the isotopic variations of MORB from IFZ-GFZ indicate that the contribution of plume materials is mainly restricted at segment 27 while barely affects the surrounding segments, in agreement with sharp decreases in crustal thickness adjacent to segment 27 (Figure 3a) [*Niu et al.*, 2015]. Therefore, the source compositions of the high-Al MORB can be modeled. As high-Al and Main MORB show generally parallel REE patterns and spider diagrams, we assume that the Crozet plume materials after previous melt extraction would have similarly depleted trace elemental compositions as normal depleted mantle for Main MORB. Considering the Crozet hotspot have two different chemical compositions, we use a simple 3-end-member mixing model to estimate their relative proportions and the modeling end-members are averages for Main MORB from segment 27 representing preexisting asthenospheric mantle compositions without the contribution of the Crozet hotspot, basalts from the western Crozet islands, and basalts from the eastern Crozet islands, respectively. Quantitative modeling suggests that the compositions of these samples can be generated by melting of a mantle source consisting of ~30–50% preexisting asthenospheric mantle together with 50–70% Crozet hotspot materials (Figure 9). Thus, both geochemical and geophysical observations can be explained by interaction of the Crozet hotspot and SWIR.

6.2. Constraints on Segment-Scale Crustal Accretion

Different from fast-spreading ridges where crustal thickness is relatively uniform at most segments, segment-scale melt supply at ultraslow-spreading ridges has been known to be highly variable with dramatic changes in crustal thickness and MORB chemistry [e.g., *Cannat et al.*, 2008; *Carbotte et al.*, 2015; *Standish et al.*, 2008]. As crustal thickness is the total melt production rate divided by full spreading rate [*Maclennan et al.*, 2001], and almost the entire SWIR spreads at a constant rate of

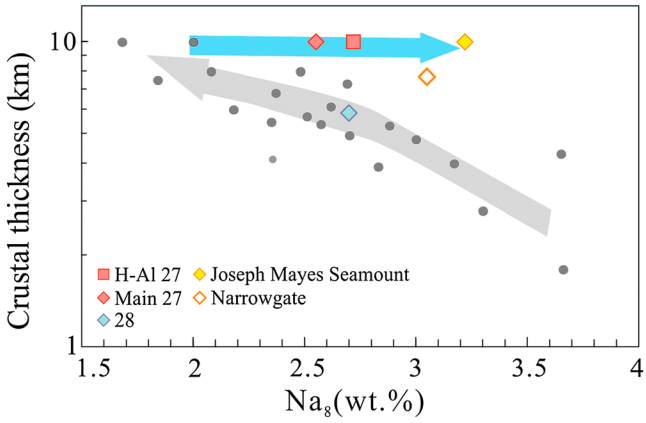

Figure 10. Segment averages of seismically determined crustal thickness versus Na_8 (Na_2O content of basalts normalized to 8 wt % MgO) [*Klein and Langmuir*, 1987] along MOR globally (grey dots) and for segments from the SWIR. The grey arrows represent global correlations suggesting the coupling of thicker crust and higher degree of partial melting (lower Na_8). It is clearly shown here the segments with thick crust at the ultraslow-spreading SWIR do not follow the trend, with much higher Na_8 values (lower partial melting degrees) at comparable crustal thickness (blue arrow). Global data are from *White and Klein* [2014, and references therein]. Sources for crustal thickness for segments 27 and 28 are from *Niu et al.* [2015], and data for the Joseph Mayes Seamount and Narrowgate are all from *Standish et al.* [2008].

14 mm/yr [*Horner-Johnson et al.*, 2005], crustal thickness variations directly reflect differences in the melt production rates beneath the ridges. Chemical indicators of extents of melting, Na_8, are known to correlate with crustal thickness at a global scale (Figure 10) [*Klein and Langmuir*, 1987]. Systematically lower Na_8 for MORB from IFZ-GFZ (2.61 wt % on average) than those from 52 to 65°E (up to 3.89 wt %) was also proposed to indicate enhanced melt supply beneath the IFZ-GFZ, consistent with shallower axial depth of the former [*Cannat et al.*, 2008]. However, MORB from segment 27 have generally comparable Na_8 values with those from segment 28 despite of the 4.4 km disparity in crustal thickness (Figure 10) [*Niu et al.*, 2015], and moreover, MORB from the Joseph Mayes Seamount have even higher Na_8 than MORB from both segment 27 and elsewhere with similar crustal thickness of ~10 km (Figure 10), inconsistent with the global correlation. We argue that such variations reflect different regional- and segment-scale melt supply beneath ultraslow-spreading ridges. Regional (>200 km) melt supply variations could directly reflect flow and melting in the subaxial asthenospheric mantle [*Cannat et al.*, 2008], thus exhibiting good correlations of partial melting degrees (Na_8) with seismically estimated crustal thickness. However, segment-scale melt supply variations (<200 km) are more complicated, possibly including the effects of along-axis and/or across-axis melt transport and redistribution at the base of, or within the axial lithosphere [e.g., *Cannat et al.*, 2008; *Standish et al.*, 2008], and thus would result in the decoupling of Na_8 and crustal thickness (Figure 10). All the segments within the IFZ-GFZ are generally magma-robust segments among the entire SWIR with less variable spreading geometry compared with the 11°E and 15°E SWIR [*Cannat et al.*, 2008]; thus, considerable along-axis melt redistribution from adjacent segments to segment 27 like that proposed for the accretion of the Joseph Mayes Seamount seems implausible. Therefore, we suggest that the enhanced melt supply beneath segment 27 mainly reflect additional flux of the Crozet plume material into the melting region.

Almost half of the samples collected from segment 27 are Main MORB with similar chemical compositions with MORB from nearby segments (Figures 2–4 and 6), suggesting they formed by partial melting of the same source, most likely the ambient asthenospheric mantle. The other half (8 out of 15), on the other hand, are isotopically enriched high-Al N-MORB largely sourced from the Crozet hotspot materials. The crust at segment 27 is up to 10.2 km thick at the center, almost twice as thick as segment 28 (5.8 km [*Niu et al.*, 2015]). Although the current sample set is too small to represent the relative proportions of two magmas beneath the ridge, the coincidence of the sudden increase of crustal thickness and the presence of the high-Al MORB only at this location suggest that the 4.4 km difference of crustal thickness between the two segments might result from the contribution of the Crozet hotspot materials. The absence of such high-Al MORB with enriched Crozet-like isotopic compositions in nearby segments suggested the NTDs surrounding segment 27 might behave as barriers preventing magma flows to nearby segments, consistent with the abruptly thinning crustal thickness to <6 km for the NTD and segment 28 to the west [*Li et al.*, 2015; *Niu et al.*, 2015]. Such sample distribution also support the hypothesis that melt delivery are highly focused beneath segment 27 along a steeply dipping permeability barrier at the base of lithosphere as proposed by *Li et al.* [2015].

High-Al MORB have slightly higher $(La/Sm)_N$ ratios (0.52–0.56) and Na_8 (2.5–2.95 wt %) than the Main MORB (0.39–0.43, 2.48–2.64 wt %) erupted at segment 27 (Figures 5 and 10). A possible explanation comes from a

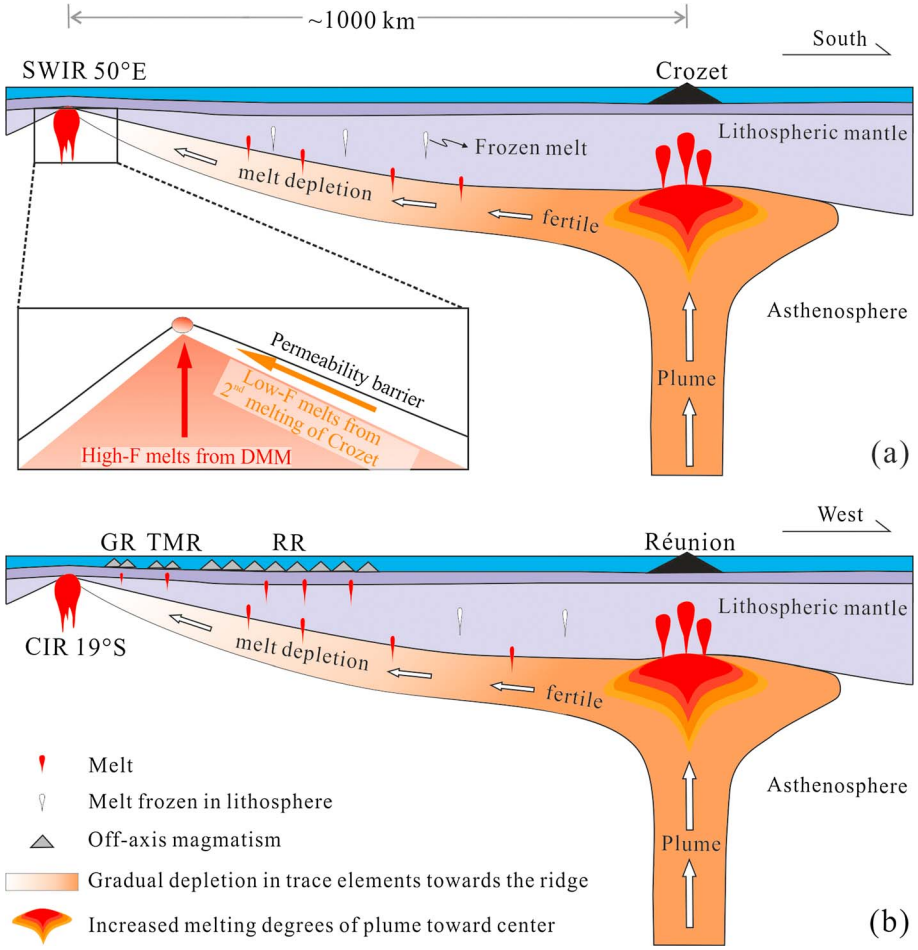

Figure 11. Simplified models for plume-ridge interactions with plume-ridge distance of around 1000 km for (a) the Crozet hotspot with the SWIR and (b) the Réunion hotspot with the Central Indian Ridge (CIR) (not to scale). During interaction of an off-axis plume with the MOR, decompression melting would occur along the upslope flow path of the plume materials. The resulting melt could either be "frozen" in the thick lithosphere (most likely the case for the SWIR) (Figure 11a) or erupt to form off-axis magmatism as seen by the off-axis magmatism near CIR, including the Gasitao Ridge (GR), Three Magi Ridge (TMR), and Rodrigues Ridge (RR) (Figure 11b). Thus, such low-degree melt extractions along the path would gradually deplete the plume material in incompatible elements but not significantly change the isotopic compositions, and the materials eventually contributing to the MOR after the long transportation would be trace elemental depleted to produce isotopically enriched N-MORB. The insert in Figure 11a schematically show the melting regime beneath segment 27. The Crozet plume materials migrating laterally and upward along the permeability barrier beneath MOR would begin to remelt at the edge of the melting regime and produce low-degree melts, while the DMM flowing upward to the center of the melting regime generate slightly higher-F melts.

consideration of the geometry of the triangle melting regime, coupled with the proposal of melt extraction through high-porosity channels at the base of the lithosphere [e.g., *Hebert and Montési*, 2010, and references therein] (insert in Figure 11a). It is important to note that in such a triangle melting regime, mantle at the edges always melts to a lower degree than that at the center. Thus, the Crozet plume materials migrating laterally and upward along the dipping lithosphere beneath MOR would begin to melt at the edge of the melting regime and produce melts with slightly lower partial melting degrees (high-Al MORB) than the DMM flowing upward to the center of the melting regime (Main MORB) (insert in Figure 11a). Furthermore, the slightly lower $(La/Sm)_N$ and Na_8 of Main MORB from segment 27 than that from nearby segments (Figures 5 and 10) also suggest that extra heat from the plume materials, might also help to enhance the partial melting degrees of normal asthenospheric mantle beneath segment 27. Such an effect of plume materials heating ambient mantle during off-axis plume-ridge interaction has been supported by numerical studies [*Hall and Kincaid*, 2004].

After melt extraction from the melting regime, the melts were subsequently transported along high-porosity channels beneath the permeability barrier to the crust. Possible mixing of the two magmas from the hotspot and DMM beneath segment 27 could then occur during (1) melt extraction in the mantle when DMM melts flow upward to high-porosity channels where most of the plume melts are and (2) magma transportation in the lower crust. But the distribution of two magma suites with distinct elemental and isotopic compositions at the same segment center indicates they might follow different paths to have varied assimilation history and prevent effective mixing between them. *Carbotte et al*. [2015] suggested that under ultraslow-spreading ridges, crustal magma bodies formed within a segment are more localized and ephemeral than at fast-spreading ridges: melt mush and melt lenses may develop at various levels in the crust and upper mantle lithosphere along the segment. Thus, the two suites of magma are likely hosted in different magma lenses to avoid mixing, and subsequent magma eruption would tap those lenses discretely. Such discrete eruptions have also been proposed for the Lucky Strike [*Gale et al*., 2011] where volcanic activities was suggested to be caused by highly focused magma bodies creating sporadic intrusions into the shallow ocean crust [*Dziak et al*., 2004].

We emphasize here that while geophysical data present a time-averaged view of crustal construction, geochemical analyses of individual lavas represent a snapshot in time of only a small fraction of the melt that over time will build the crust [*Carbotte et al*., 2015]. Thus, future studies about the temporal variations of MORB erupted at segment 27 would potentially provide a more comprehensive view about the accretion of the ultrathick crust.

6.3. General Implications for Off-Axis Plume-Ridge Interaction

It is widely acknowledged that typical plume-ridge interaction would generate E-MORB on the ridge axis [e.g., *Ito et al*., 2003; *Schilling*, 1973], however, the identification of isotopically enriched N-MORB in this study provides a different perspective that plume-ridge interaction could also produce N-MORB.

6.3.1. Global Distribution of Isotopically Enriched N-MORB

During interaction of an off-axis plume with the MOR, decompression melting was proposed to occur along the upslope flow path of the plume materials, which might then melt again under further decompression beneath a MOR [*Hall and Kincaid*, 2003, 2004; *Sleep*, 1996]. Therefore, the plume materials after melt extraction along the flow path would form a special mantle end-member elementally depleted but isotopically enriched and complicate the source heterogeneity of MORB. However, isotopically enriched N-MORB are not common among MOR globally. To study their global distributions we filtered compiled global MORB data [*Class and Kerstin*, 2012; *Gale et al*., 2013a] with criteria of chondrite-normalized ratios $(La/Sm)_N < 0.7$ and $^{143}Nd/^{144}Nd < 0.5130$ and only 31 samples are within this category (Figure 7 and Data Set S2 in the supporting information). These MORB samples show a totally different trend compared to the commonly coupled enrichment/depletion of trace elements and isotopes for both global MORB and MORB from ridge segments within 200 km of a hotspot (Figure 7). Such decoupling of trace element and isotopic characteristics reflect a special mantle process to form a trace elemental depleted but isotopically less depleted source. And these processes were documented worldwide, e.g., the SWIR, Central Indian Ridge (CIR), Southeast Indian Ridge, and South Atlantic Ridge. Most interestingly, these isotopically enriched N-MORB might all be genetically related to possible interaction of ridge with off-axis plumes (Data Set S2). Isotopically enriched N-MORB from the South Atlantic Ridge was explained to be related to the partial melting and dispersion of the Tristan and St. Helena residue plume material into the asthenosphere [*Douglass et al*., 1999; *Fontignie and Schilling*, 1996; *Hanan et al*., 1986], similar to our interpretations.

Among these isotopically enriched N-MORB, on-axis (one sample) and off-axis (four samples, the Gasitao Ridge) MORB from the CIR are most interesting because only isotopically enriched N-MORB were collected in these locations with the absence of typical E-MORB, whereas the E-MORB present to the north of the isotopically enriched N-MORB are not consistent with the contribution of the Réunion hotspot both chemically and isotopically [*Nauret et al*., 2006], similar to the setting at the IFZ-GFZ section. The Réunion hotspot is located more than 1000 km to the west of the CIR (19–20°S). Off-axis structures in this plume-ridge interval have been recognized and referred to as the Rodrigues, Three Magi, and Gasitao Ridges from west to east (detailed bathymetric map and geological settings are as described in *Nauret et al*. [2006]). Rodrigues Ridge basalts vary from E-MORB to N-MORB with decreasing $(La/Sm)_N$ ratios but constant isotopic compositions from west to east suggesting diminishing influences of the Réunion hotspot toward the CIR

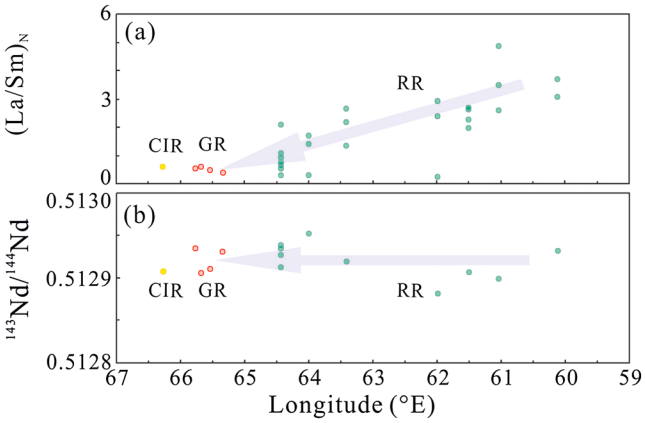

Figure 12. Plots of $(La/Sm)_N$ and $^{143}Nd/^{144}Nd$ versus Longitude for basalts between the Réunion hotspot (the right end) and Central Indian Ridge (CIR). The arrows show the trends toward lower $(La/Sm)_N$ but constant $^{143}Nd/^{144}Nd$ ratios with increased distances away from the Réunion hotspot, indicating basalts have gradually depleted trace elemental compositions but similarly enriched isotopic compositions further from the hotspot. Such a distribution of samples from E-MORB to isotopic enriched N-MORB is best evidence for the model proposed in Figure 11b. Data are from *Mellor* [1998] for the RR samples and from *Nauret et al*. [2006] for the GR and CIR samples. Geographic locations of these basalts can be found in *Mellor* [1998] and *Nauret et al*. [2006].

(Figure 12) [*Mellor*, 1998]. Basalts collected farther to the east at the Gasitao Ridge were all N-MORB which resemble Réunion hotspot in terms of Sr-Nd-Pb-He isotopes [*Füri et al*., 2011; *Nauret et al*., 2006], and one sample collected from 19 to 20°S CIR is also the similarly isotopically enriched N-MORB (Figure 12) [*Nauret et al*., 2006]. Melting residue of Réunion hotspot materials has been proposed as a source end-member for these isotopically enriched N-MORB [*Füri et al*., 2011]. Therefore, such a distribution of geochemically varying MORB samples is a strong evidence to show that the enriched mantle part of the distal Réunion hotspot material was exhausted beneath the Rodrigues Ridge, whereas the depleted residue after melt extraction migrates farther through the Gasitao Ridge to the CIR to produce the isotopically enriched N-MORB at the Gasitao Ridge and CIR (Figure 11b).

Other interesting similarities between these isotopically enriched N-MORB include the following: (1) most of them have DUPAL anomaly (an isotopic anomaly from DUPré and ALlègre [*Dupré and Allègre*, 1983], Figure S3) and (2) those samples with MgO higher than 8 wt % mostly have higher Al_2O_3 than 16 wt % with $(Sr/Nd)_N$ higher than 1 (Data Set S2). Are they just a coincidence, or could they reflect special mantle and/or crustal processes for the genesis of such plume-influenced MORB? The factors behind these observations are beyond the scope of this paper but worth detailed investigations in the future.

6.3.2. Controls of Plume-Ridge Distance and Spreading Rate on Off-Axis Plume-Ridge Interactions

The "expression" and "intensity" of geochemical consequences of plume-ridge interaction are known to vary systematically with the plume-ridge distance [*Niu and Hekinian*, 2004], but inversely with the spreading rate of the ridge [*Ito and Lin*, 1995; *Ribe*, 1996]. Most of the isotopically enriched N-MORB were found at slower-spreading ridges with large plume-ridge distances, except for two samples from the fast-spreading Easter Microplate East Rift and Pacific-Antarctic Ridge (Data Set S2). Such a distribution may be ascribed to the control of both plume-ridge distance and spreading rate on the interaction between off-axis plume and MOR.

For on-axis plumes like Iceland, fertile plume materials would directly contribute to the MOR and melt to produce both elementally and isotopically enriched MORB. However, for off-axis plume-ridge interactions, plume materials would undergo decompression and therefore melting en route to the ridge due to shallower lithosphere-asthenosphere boundary closer to the ridge [*Hall and Kincaid*, 2003, 2004; *Sleep*, 1996]. The resulting melt could either freeze in the thick lithosphere (most likely the case for the SWIR, Figure 11a) or erupt to form off-axis edifices as seen by the volcanic lineaments between the Réunion hotspot and CIR (Figure 11b) [*Füri et al*., 2011]. For off-axis plumes with a relatively short plume-ridge distance, the effect of such pressure-release melting on the chemical compositions of the plume materials as a whole might be insignificant, and thus, fertile mantle could still contribute to ridge magmatism. However, for distal plumes with plume-ridge distances around 1000 km, continuous decompression melting along such a long path would considerably deplete the plume material in incompatible elements but not change the isotopic compositions (for a homogeneous plume). Therefore, when they finally reach the ridge, the depleted residue might remelt due to further decompression at MOR and produce isotopically enriched N-MORB. Such a process is best evidenced by decreasing $(La/Sm)_N$ ratios but constant $^{143}Nd/^{144}Nd$ of basalts from the Réunion to CIR (Figure 12). The restricted distribution of isotopically enriched N-MORB only at segment 27 at SWIR and CIR 19°S suggest that

the off-axis plume most likely communicate with the ridge through a narrow, subhorizontal conduit, in agreement with previous experimental results by *Kincaid et al*. [1995]. The presence or absence of off-axis volcanic lineaments between the plume and ridge could be explained by varied lithosphere ages beneath the hotspots [*Mittelstaedt and Ito*, 2005; *Sauter et al*., 2009]. Upwelling of plume materials was proposed to cause lithospheric tension on younger lithosphere (<25 Ma, e.g., the lithosphere beneath the Réunion hotspot) or with plume-ridge distance of < 1250 km to promote volcanic lineament formation, but the plate beneath the Crozet hotspot (sitting on a Late Cretaceous lithosphere) may be too thick for plume stresses to enhance the ability of magma to penetrate the plate [*Mittelstaedt and Ito*, 2005; *Sauter et al*., 2009].

Furthermore, at fast-spreading ridges, melts from such a mantle end-member would be easily mixed with and diluted by abundant melts from DMM in the magma mush, whereas at slower-spreading ridges such as the SWIR and CIR where the melt supply are limited, heterogeneous mantle compositions can be better preserved in the erupted MORB. Also, highly focused mantle melt beneath slow- and ultraslow-spreading ridges [e.g., *Carbotte et al*., 2015] would likely concentrate the melt from heterogeneous mantle sources to a relatively small scale of ridge segments compared with generally smooth lithosphere base beneath fast-spreading ridges; i.e., the occurrence of isotopically enriched N-MORB are only limited within segment 27 along the IFZ-GFZ region.

The maximum distance for possible plume-ridge interaction to occur has been controversial, from hundreds of kilometers [e.g., *Ito and Lin*, 1995; *Kincaid et al*., 1996; *Sleep*, 1996] to over 1000 km [e.g., *Schilling*, 1991; *Mittelstaedt and Ito*, 2005]. Such distances are also believed to increase with slower-spreading rate. Numerical modeling by *Kincaid et al*. [1996] suggests that as separation distance increases to > 600 km, only slow-spreading ridges are predicted to be able to experience plume-to-ridge communication, which actually correlates with the global distribution of isotopic enriched N-MORB most at slower-spreading ridges with large plume-ridge distances. Combined with the strong chemical evidence to support such a plume-ridge interaction over 1000 km between the Réunion hotspot with CIR (Figure 12), we infer that the plume-ridge distance of around 1000 km might be considered as a critical distance where E-MORB would not be produced at slow to ultraslow-spreading ridges influenced by hotspots. That is, plume materials might still contribute to MOR magmatism with larger plume-ridge distances, but in a different version: melting residue instead of fertile plume mantle, and with different chemical expressions: isotopically enriched N-MORB, not E-MORB.

7. Conclusions

1. Isotopically enriched N-MORB are identified from the Southwest Indian Ridge (SWIR) at 50°28′E with anomalously thick crust. These new samples provide necessary geochemical evidence for the interaction between the Crozet hotspot and SWIR. Their only presence at 50°28′E indicates that the contribution of Crozet plume material is only restricted to the individual segment and melt delivery beneath the ultraslow-spreading Southwest Indian Ridge is highly focused.
2. The distribution of isotopically enriched N-MORB globally is mostly associated with hotspots, suggesting a possible genetic relationship between them. In particular, the constant Nd isotopic compositions with decreasing $(La/Sm)_N$ ratios for off-axis magmatism between the Réunion hotspot toward the CIR are best evidence for a similar off-axis plume-ridge interaction model. We propose that during interaction of an off-axis plume with the MOR, decompression melting would occur along the upslope flow path of the plume materials. The resulting melt could either freeze in the thick lithosphere (most likely the case for the SWIR) or erupt to form off-axis edifices like the volcanic lineaments between the Réunion hotspot and CIR. Thus, such a low-degree melt extraction would deplete the plume material in incompatible elements but not significantly change the isotopic compositions, and when they finally reach the ridge, the depleted residue would remelt due to further decompression at MOR and produce isotopically enriched N-MORB.
3. Isotopically enriched N-MORB mostly occur at slower-spreading ridges with large plume-ridge distances (around 1000 km). Large plume-ridge distances would enhance low-degree melt extraction during the migration of plume materials to the ridge. Also, unique chemical signatures of depleted plume residue would be better preserved in the MORB from slower-spreading with lower melt supply and thus lower degree of mixing in the magma mush. We infer that plume materials might still contribute to MOR

magmatism with plume-ridge distances larger than 1000 km for slow to ultraslow-spreading ridges, but in a different version: melting residue instead of fertile plume mantle, and with different chemical expressions: isotopically enriched N-MORB, not E-MORB.

Acknowledgments

This study was funded by projects from the Natural Science Foundation of China (41403027 and 40873020), China Ocean Mineral Resources R&D Association (DY125-11-R-06), and Research Grant Council of Hong Kong (HKU 706413P). The authors are grateful to China Ocean Sample Repository for providing SWIR samples. Ying Liu, Guangqian Hu, Jinlong Ma, Le Zhang, and Fukun Chen helped with major and trace element and isotopic analyses. The manuscript benefited greatly from discussions with Weidong Sun and Changming Xing. We are grateful to Michael Walter, Emily M. Klein, and Minghui Zhao for their careful and constructive comments which significantly improved the manuscript. The data used are listed in the tables, references, and supporting information. Data sets and additional figures noted in the main text can be found in the supporting information. This is contribution IS-2323 from GIGCAS.

References

Baker, J., D. Peate, T. Waight, and C. Meyzen (2004), Pb isotopic analysis of standards and samples using a 207Pb–204Pb double spike and thallium to correct for mass bias with a double-focusing MC-ICP-MS, *Chem. Geol.*, *211*(3–4), 275–303, doi:10.1016/j.chemgeo.2004.06.030.

Bown, J. W., and R. S. White (1994), Variation with spreading rate of oceanic crustal thickness and geochemistry, *Earth Planet. Sci. Lett.*, *121*(3–4), 435–449, doi:10.1016/0012-821X(94)90082-5.

Breton, T., F. Nauret, S. Pichat, B. Moine, M. Moreira, E. F. Rose-Koga, D. Auclair, C. Bosq, and L.-M. Wavrant (2013), Geochemical heterogeneities within the Crozet hotspot, *Earth Planet. Sci. Lett.*, *376*, 126–136, doi:10.1016/j.epsl.2013.06.020.

Cannat, M., C. Rommevaux-Jestin, D. Sauter, C. Deplus, and V. Mendel (1999), Formation of the axial relief at the very slow spreading Southwest Indian Ridge (49° to 69°E), *J. Geophys. Res.*, *104*(B10), 22,825–22,843, doi:10.1029/1999JB900195.

Cannat, M., D. Sauter, A. Bezos, C. Meyzen, E. Humler, and M. Le Rigoleur (2008), Spreading rate, spreading obliquity, and melt supply at the ultraslow spreading Southwest Indian Ridge, *Geochem. Geophys. Geosyst.*, *9*, Q04002, doi:10.1029/2007GC001676.

Cantagrel, J., J. Lameyre, and J. Nougier (1980), Volcanologie et géochronologie d'une île volcanique, île de l'Est (archipel de Crozet), 26e Congrès International de Géologie, 27.

Carbotte, S. M., D. K. Smith, M. Cannat, and E. M. Klein (2015), Tectonic and magmatic segmentation of the Global Ocean Ridge System: A synthesis of observations, *Geol. Soc. London, Spec. Publ.*, *420*, doi:10.1144/SP420.5.

Chernyshev, I., A. Chugaev, and K. Shatagin (2007), High-precision Pb isotope analysis by multicollector-ICP-mass-spectrometry using 205Tl/203Tl normalization: Optimization and calibration of the method for the studies of Pb isotope variations, *Geochem. Int.*, *45*(11), 1065–1076.

Class, C. L., and Kerstin (2012), PetDB expert MORB (mid-ocean ridge basalt) compilation, *EarthChem Lib.*, doi:10.1594/IEDA/100060.

Cushman, B., J. Sinton, G. Ito, and J. Eaby Dixon (2004), Glass compositions, plume-ridge interaction, and hydrous melting along the Galápagos Spreading Center, 90.5°W to 98°W, *Geochem. Geophys. Geosyst.*, *5*, Q08E17, doi:10.1029/2004GC000709.

Danyushevsky, L. V., M. R. Perfit, S. M. Eggins, and T. J. Falloon (2003), Crustal origin for coupled "ultra-depleted" and "plagioclase" signatures in MORB olivine-hosted melt inclusions: Evidence from the Siqueiros Transform Fault, East Pacific Rise, *Contrib. Mineral. Petrol.*, *144*(5), 619–637.

Danyushevsky, L. V., R. A. J. Leslie, A. J. Crawford, and P. Durance (2004), Melt inclusions in primitive olivine phenocrysts: The role of localized reaction processes in the origin of anomalous compositions, *J. Petrol.*, *45*(12), 2531–2553, doi:10.1093/petrology/egh080.

Douglass, J., J. G. Schilling, and D. Fontignie (1999), Plume-ridge interactions of the Discovery and Shona mantle plumes with the southern Mid-Atlantic Ridge (40–55 S), *J. Geophys. Res.*, *104*(B2), 2941–2962, doi:10.1029/98JB02642.

Dupré, B., and C. J. Allègre (1983), Pb-Sr isotope variation in Indian Ocean basalts and mixing phenomena, *Nature*, *303*(5913), 142–146.

Dziak, R. P., D. K. Smith, D. R. Bohnenstiehl, C. G. Fox, D. Desbruyeres, H. Matsumoto, M. Tolstoy, and D. J. Fornari (2004), Evidence of a recent magma dike intrusion at the slow spreading Lucky Strike segment, Mid-Atlantic Ridge, *J. Geophys. Res.*, *109*, B12102, doi:10.1029/2004JB003141.

Eason, D., and J. Sinton (2006), Origin of high-Al N-MORB by fractional crystallization in the upper mantle beneath the Galápagos Spreading Center, *Earth Planet. Sci. Lett.*, *252*(3), 423–436.

Fontignie, D., and J.-G. Schilling (1996), Mantle heterogeneities beneath the South Atlantic: A Nd Sr Pb isotope study along the Mid-Atlantic Ridge (3°S–46°S), *Earth Planet. Sci. Lett.*, *142*(1), 209–221.

Füri, E., D. R. Hilton, B. J. Murton, C. Hémond, J. Dyment, and J. M. D. Day (2011), Helium isotope variations between Réunion Island and the Central Indian Ridge (17°–21°S): New evidence for ridge–hot spot interaction, *J. Geophys. Res.*, *116*, B02207, doi:10.1029/2010JB007609.

Gale, A., S. Escrig, E. J. Gier, C. H. Langmuir, and S. L. Goldstein (2011), Enriched basalts at segment centers: The Lucky Strike (37°17′N) and Menez Gwen (37°50′N) segments of the Mid-Atlantic Ridge, *Geochem. Geophys. Geosyst.*, *12*, Q06016, doi:10.1029/2010GC003446.

Gale, A., C. A. Dalton, C. H. Langmuir, Y. Su, and J.-G. Schilling (2013a), The mean composition of ocean ridge basalts, *Geochem. Geophys. Geosyst.*, *14*, 489–518, doi:10.1029/2012GC004334.

Gale, A., M. Laubier, S. Escrig, and C. H. Langmuir (2013b), Constraints on melting processes and plume-ridge interaction from comprehensive study of the FAMOUS and North Famous segments, Mid-Atlantic Ridge, *Earth Planet. Sci. Lett.*, *365*, 209–220, doi:10.1016/j.epsl.2013.01.022.

Gale, A., C. H. Langmuir, and C. A. Dalton (2014), The global systematics of ocean ridge basalts and their origin, *J. Petrol.*, *55*(6), 1051–1082.

Gautheron, C., M. Moreira, C. Gerin, L. Tassan-Got, A. Bezos, and E. Humler (2015), Constraints on the DUPAL anomaly from helium isotope systematics in the Southwest Indian mid-ocean ridge basalts, *Chem. Geol.*, *417*, 163–172.

Georgen, J. E., J. Lin, and H. J. B. Dick (2001), Evidence from gravity anomalies for interactions of the Marion and Bouvet hotspots with the Southwest Indian Ridge: Effects of transform offsets, *Earth Planet. Sci. Lett.*, *187*(3–4), 283–300, doi:10.1016/s0012-821x(01)00293-x.

Ghiorso, M. S., and R. O. Sack (1995), Chemical mass transfer in magmatic processes IV: A revised and internally consistent thermodynamic model for the interpolation and extrapolation of liquid-solid equilibria in magmatic systems at elevated temperatures and pressures, *Contrib. Mineral. Petrol.*, *119*(2), 197–212.

Goslin, J., M. Recq, and R. Schlich (1981), Structure profonde du plateau de Madagascar: Relations avec le plateau de Crozet, *Tectonophysics*, *76*(1), 75–97.

Hall, P. S., and C. Kincaid (2003), Melting, dehydration, and the dynamics of off-axis plume-ridge interaction, *Geochem. Geophys. Geosyst.*, *4*(9), 8510, doi:10.1029/2003GC000567.

Hall, P. S., and C. Kincaid (2004), Melting, dehydration, and the geochemistry of off-axis plume-ridge interaction, *Geochem. Geophys. Geosyst.*, *5*, Q12E18, doi:10.1029/2003GC000667.

Hanan, B., R. Kingsley, and J.-G. Schilling (1986), Pb isotope evidence in the South Atlantic for migrating ridge-hotspot interactions, *Nature*, *322*, 137–144.

Hebert, L. B., and L. G. Montési (2010), Generation of permeability barriers during melt extraction at mid-ocean ridges, *Geochem. Geophys. Geosyst.*, *11*, Q12008, doi:10.1029/2010GC003270.

Horner-Johnson, B. C., R. G. Gordon, S. M. Cowles, and D. F. Argus (2005), The angular velocity of Nubia relative to Somalia and the location of the Nubia—Somalia–Antarctica triple junction, *Geophys. J. Int.*, *162*(1), 221–238.

Ito, G., and J. Lin (1995), Oceanic spreading center–hotspot interactions: Constraints from along-isochron bathymetric and gravity anomalies, *Geology*, *23*(7), 657–660.

Ito, G., J. Lin, and D. Graham (2003), Observational and theoretical studies of the dynamics of mantle plume–mid-ocean ridge interaction, *Rev. Geophys.*, *41*(4), 1017, doi:10.1029/2002RG000117.

Janney, P. E., A. P. Le Roex, and R. W. Carlson (2005), Hafnium isotope and trace element constraints on the nature of mantle heterogeneity beneath the central Southwest Indian Ridge (13°E to 47°E), *J. Petrol.*, *46*(12), 2427–2464, doi:10.1093/petrology/egi060.

Jokat, W., and M. C. Schmid-Aursch (2007), Geophysical characteristics of the ultraslow spreading Gakkel Ridge, Arctic Ocean, *Geophys. J. Int.*, *168*(3), 983–998.

Jokat, W., O. Ritzmann, M. Schmidt-Aursch, S. Drachev, S. Gauger, and J. Snow (2003), Geophysical evidence for reduced melt production on the Arctic ultra-slow Gakkel mid-ocean ridge, *Nature*, *423*, 962–965.

Kamenetsky, V. S., S. M. Eggins, A. J. Crawford, D. H. Green, M. Gasparon, and T. J. Falloon (1998), Calcic melt inclusions in primitive olivine at 43°N MAR: Evidence for melt–rock reaction/melting involving clinopyroxene-rich lithologies during MORB generation, *Earth Planet. Sci. Lett.*, *160*(1), 115–132.

Kincaid, C., G. Ito, and C. Gable (1995), Laboratory investigation of the interaction of off-axis mantle plumes and spreading centres, *Nature*, *376*(6543), 758–761.

Kincaid, C., J.-G. Schilling, and C. Gable (1996), The dynamics of off-axis plume-ridge interaction in the uppermost mantle, *Earth Planet. Sci. Lett.*, *137*(1), 29–43.

Klein, E. M., and C. H. Langmuir (1987), Global correlations of ocean ridge basalt chemistry with axial depth and crustal thickness, *J. Geophys. Res.*, *92*(B4), 8089–8115, doi:10.1029/JB092iB08p08089.

Klein, E. M., C. H. Langmuir, and H. Staudigel (1991), Geochemistry of basalts from the southeast Indian Ridge, 115°E–138°E, *J. Geophys. Res.*, *96*(B2), 2089–2107, doi:10.1029/90JB01384.

Langmuir, C. H., and J. F. Bender (1984), The geochemistry of oceanic basalts in the vicinity of transform faults: Observations and implications, *Earth Planet. Sci. Lett.*, *69*(1), 107–127.

Laubier, M., A. Gale, and C. H. Langmuir (2012), Melting and Crustal Processes at the FAMOUS Segment (Mid-Atlantic Ridge): New Insights from Olivine-hosted Melt Inclusions from Multiple Samples, *J. Petrol.*, *53*(4), 665–698, doi:10.1093/petrology/egr075.

le Roux, P. J., A. P. le Roex, J. G. Schilling, N. Shimizu, W. W. Perkins, and N. J. G. Pearce (2002), Mantle heterogeneity beneath the southern Mid-Atlantic Ridge: Trace element evidence for contamination of ambient asthenospheric mantle, *Earth Planet. Sci. Lett.*, *203*(1), 479–498, doi:10.1016/s0012-821x(02)00832-4.

Lehnert, K., Y. Su, C. Langmuir, B. Sarbas, and U. Nohl (2000), A global geochemical database structure for rocks, *Geochem. Geophys. Geosyst.*, *1*(5), 1012, doi:10.1029/1999GC000026.

Li, J., H. Jian, Y. J. Chen, S. C. Singh, A. Ruan, X. Qiu, M. Zhao, X. Wang, X. Niu, and J. Ni (2015), Seismic observation of an extremely magmatic accretion at the ultraslow spreading Southwest Indian Ridge, *Geophys. Res. Lett.*, *42*, 2656–2663, doi:10.1002/2014GL062521.

Li, X. H., D. Liu, M. Sun, W. Li, X. R. Liang, and Y. Liu (2004), Precise Sm–Nd and U–Pb isotopic dating of the supergiant Shizhuyuan polymetallic deposit and its host granite, SE China, *Geol. Mag.*, *141*(2), 225–231.

Li, X. H., Z. X. Li, M. T. D. Wingate, S. L. Chung, Y. Liu, G. C. Lin, and W. X. Li (2006), Geochemistry of the 755 Ma Mundine Well dyke swarm, northwestern Australia: Part of a Neoproterozoic mantle superplume beneath Rodinia?, *Precambrian Res.*, *146*(1), 1–15.

Lissenberg, C. J., and H. J. B. Dick (2008), Melt-rock reaction in the lower oceanic crust and its implications for the genesis of mid-ocean ridge basalt, *Earth Planet. Sci. Lett.*, *271*(1–4), 311–325, doi:10.1016/j.epsl.2008.04.023.

Liu, Y., H. C. Liu, and X. H. Li (1996), Simultaneous and precise determination of 40 trace elements in rock samples using ICP-MS, edited, pp. 552–558, Geochimica.

Maclennan, J., D. McKenzie, K. Gronvöld, and L. Slater (2001), Crustal accretion under northern Iceland, *Earth Planet. Sci. Lett.*, *191*(3–4), 295–310, doi:10.1016/S0012-821X(01)00420-4.

Mahoney, J. J., W. M. White, B. G. J. Upton, C. R. Neal, and R. A. Scrutton (1996), Beyond EM-1: Lavas from Afanasy-Nikitin rise and the Crozet archipelago, Indian Ocean, *Geology*, *24*(7), 615–618, doi:10.1130/0091-7613(1996)024<0615:belfan>2.3.co;2.

Mahoney, J., A. P. Leroex, Z. Peng, R. L. Fisher, and J. H. Natland (1992), Southwestern limits of Indian Ocean ridge mantle and the origin of low 206Pb/204Pb Mid-ocean ridge basalt: Isotope systematics of the Central Southwest Indian Ridge (17°–50°E), *J. Geophys. Res.*, *97*(B13), 19,771–19,790, doi:10.1029/92JB01424.

McDonough, W. F., and S. S. Sun (1995), The composition of the Earth, *Chem. Geol.*, *120*(3–4), 223–253.

Mellor, S. H. (1998), *The Geochemistry and Petrology of the Rodrigues Ridge (Western Indian Ocean)*, Univ. of Greenwich, London.

Melson, W. G., and T. O'Hearn (1979), Basaltic glass erupted along the Mid-Atlantic Ridge between 0–37°N: Relationships between composition and latitude, in *Deep Drilling Results in the Atlantic Ocean: Ocean Crust*, edited by M. Talwani, C. G. Harrison, and D. E. Hayes, pp. 249–261, AGU, Washington, D. C.

Mendel, V., D. Sauter, C. Rommevaux-Jestin, P. Patriat, F. Lefebvre, and L. M. Parson (2003), Magmato-tectonic cyclicity at the ultra-slow spreading Southwest Indian Ridge: Evidence from variations of axial volcanic ridge morphology and abyssal hills pattern, *Geochem. Geophys. Geosyst.*, *4*(5), 9102, doi:10.1029/2002GC000417.

Meyzen, C. M., M. J. Toplis, E. Humler, J. N. Ludden, and C. Mevel (2003), A discontinuity in mantle composition beneath the southwest Indian ridge, *Nature*, *421*(6924), 731–733, doi:10.1038/nature01424.

Meyzen, C. M., J. N. Ludden, E. Humler, B. Luais, M. J. Toplis, C. Mevel, and M. Storey (2005), New insights into the origin and distribution of the DUPAL isotope anomaly in the Indian Ocean mantle from MORB of the Southwest Indian Ridge, *Geochem. Geophys. Geosyst.*, *6*, Q11k11, doi:10.1029/2005GC000979.

Mittelstaedt, E., and G. Ito (2005), Plume-ridge interaction, lithospheric stresses, and the origin of near-ridge volcanic lineaments, *Geochem. Geophys. Geosyst.*, *6*, Q06002, doi:10.1029/2004GC000860.

Nauret, F., W. Abouchami, S. Galer, A. Hofmann, C. Hémond, C. Chauvel, and J. Dyment (2006), Correlated trace element-Pb isotope enrichments in Indian MORB along 18–20 S, Central Indian Ridge, *Earth Planet. Sci. Lett.*, *245*(1), 137–152.

Niu, X., A. Ruan, J. Li, T. A. Minshull, D. Sauter, Z. Wu, X. Qiu, M. Zhao, Y. J. Chen, and S. Singh (2015), Along-axis variation in crustal thickness at the ultraslow spreading Southwest Indian Ridge (50°E) from a wide-angle seismic experiment, *Geochem. Geophys. Geosyst.*, *16*, 468–485, doi:10.1002/2014GC005645.

Niu, Y., and R. Hekinian (2004), Ridge suction drives plume-ridge interactions, in *Oceanic Hotspots: Intraplate Submarine Magmatism and Tectonism*, edited by R. Hékinian, P. Stoffers, and J. L. Cheminée, pp. 285–307, Springer, New York.

Reid, I., and H. Jackson (1981), Oceanic spreading rate and crustal thickness, *Mar. Geophys. Res.*, *5*(2), 165–172.
Ribe, N. (1996), The dynamics of plume-ridge interaction: 2. Off-ridge plumes, *J. Geophys. Res.*, *101*(B7), 16,195–16,204, doi:10.1029/96JB01187.
Salters, V. J. M., and W. M. White (1998), Hf isotope constraints on mantle evolution, *Chem. Geol.*, *145*(3), 447–460.
Sauter, D., P. Patriat, C. Rommevaux-Jestin, M. Cannat, A. Briais, and Gallieni Shipboard Scientific Party (2001), The Southwest Indian Ridge between 49°15′E and 57°E: Focused accretion and magma redistribution, *Earth Planet. Sci. Lett.*, *192*(3), 303–317.
Sauter, D., H. Carton, V. Mendel, M. Munschy, C. Rommevaux-Jestin, J. J. Schott, and H. Whitechurch (2004), Ridge segmentation and the magnetic structure of the Southwest Indian Ridge (at 50 30′E, 55 30′E and 66 20′E): Implications for magmatic processes at ultraslow-spreading centers, *Geochem. Geophys. Geosyst.*, *5*, Q05K08, doi:10.1029/2003GC000581.
Sauter, D., M. Cannat, C. Meyzen, A. Bezos, P. Patriat, E. Humler, and E. Debayle (2009), Propagation of a melting anomaly along the ultraslow Southwest Indian Ridge between 46°E and 52°20′E: Interaction with the Crozet hotspot?, *Geophys. J. Int.*, *179*(2), 687–699, doi:10.1111/j.1365-246X.2009.04308.x.
Schilling, J., M. Zajac, R. Evans, T. Johnston, W. White, J. Devine, and R. Kingsley (1983), Petrologic and geochemical variations along the Mid-Atlantic Ridge from 29°N to 73°N, *Am. J. Sci.*, *283*(6), 510–586.
Schilling, J.-G. (1973), Iceland mantle plume: Geochemical study of Reykjanes Ridge, *Nature*, *242*, 565–571.
Schilling, J.-G. (1991), Fluxes and excess temperatures of mantle plumes inferred from their interaction with migrating mid-ocean ridges, *Nature*, *352*(6334), 397–403, doi:10.1038/352397a0.
Slater, L., D. McKenzie, K. GRÖNVOLD, and N. Shimizu (2001), Melt generation and movement beneath Theistareykir, NE Iceland, *J. Petrol.*, *42*(2), 321–354.
Sleep, N. H. (1996), Lateral flow of hot plume material ponded at sublithospheric depths, *J. Geophys. Res.*, *101*(B12), 28,065–28,083, doi:10.1029/96JB02463.
Standish, J. J., H. J. B. Dick, P. J. Michael, W. G. Melson, and T. O'Hearn (2008), MORB generation beneath the ultraslow spreading Southwest Indian Ridge (9–25°E): Major element chemistry and the importance of process versus source, *Geochem. Geophys. Geosyst.*, *9*, Q05004, doi:10.1029/2008GC001959.
Sun, S. S., and W. McDonough (1989), Chemical and isotopic systematics of oceanic basalts: Implications for mantle composition and processes, *Geol. Soc. Spec. Publ.*, *42*(1), 313.
Tanaka, T., et al. (2000), JNdi-1: A neodymium isotopic reference in consistency with La Jolla neodymium, *Chem. Geol.*, *168*(3–4), 279–281, doi:10.1016/S0009-2541(00)00198-4.
Tao, C., J. Lin, S. Guo, Y. J. Chen, G. Wu, X. Han, C. R. German, D. R. Yoerger, N. Zhou, and H. Li (2012), First active hydrothermal vents on an ultraslow-spreading center: Southwest Indian Ridge, *Geology*, *40*(1), 47–50.
Wei, G., X. Liang, X. Li, and Y. Liu (2002), Precise measurement of Sr isotopic composition of liquid and solid base using (LP) MC-ICPMS, *Geochimica*, *31*(3), 295–299.
Weis, D., D. Weis, C. Maerschalk, J. Barling, E. Dietrich-Sainsaulieu, G. Williams, D. Hanano, J. B. Mahoney, R. Friedman, and W. Pretorius (2006), High-precision isotopic characterization of USGS reference materials by TIMS and MC-ICP-MS, *Geochem. Geophys. Geosyst.*, *7*, Q08006, doi:10.1029/2006GC001283.
Weis, D., B. Kieffer, D. Hanano, I. N. Silva, J. Barling, W. Pretorius, C. Maerschalk, and N. Mattielli (2007), Hf isotope compositions of U.S. Geological Survey reference materials, *Geochem. Geophys. Geosyst.*, *8*, Q06006, doi:10.1029/2006GC001473.
White, W., and E. Klein (2014), 4.13-Composition of the Oceanic Crust, in *Treatise on Geochemistry*, edited by H. D. Holland and K. K. Turekian, 2nd ed., pp. 457–496, Elsevier, Oxford.
Woodhead, J. D., and J. M. Hergt (2000), Pb-isotope analyses of USGS reference materials, *Geostandard Newslett*, *24*(1), 33–38, doi:10.1111/j.1751-908X.2000.tb00584.x.
Yang, A. Y., C. J. Lissenberg, and Y. Liang (2015), Reaction between MORB magma and lower oceanic crust: An experimental study, Goldschmidt Abstracts, 3498.
Zhang, T., J. Lin, and J. Y. Gao (2013), Magmatism and tectonic processes in Area A hydrothermal vent on the Southwest Indian Ridge, *Sci. China-Earth Sci.*, *56*(12), 2186–2197, doi:10.1007/s11430-013-4630-5.
Zhao, M., et al. (2013), Three-dimensional seismic structure of the Dragon Flag oceanic core complex at the ultraslow spreading Southwest Indian Ridge (49°39′E), *Geochem. Geophys. Geosyst.*, *14*, 4544–4563, doi:10.1002/ggge.20264.
Zhou, H. Y., and H. J. B. Dick (2013), Thin crust as evidence for depleted mantle supporting the Marion Rise, *Nature*, *494*(7436), 195–200, doi:10.1038/nature11842.